

Detecting Atmospheric CO₂ Trends as Population-Level Signatures for Long-Term Stable Water Oceans and Biotic Activity on Temperate Terrestrial Exoplanets

JANINA HANSEN ^{1,2} DANIEL ANGERHAUSEN ^{1,2,3,4} SASCHA P. QUANZ ^{1,2,5} DEREK VANCE ⁶
BJÖRN S. KONRAD ^{1,2} EMILY O. GARVIN ^{1,2} ELEONORA ALEI ⁷ JENS KAMMERER ⁸ AND FELIX A. DANNERT ^{1,2}

¹ETH Zurich, Institute for Particle Physics & Astrophysics, Wolfgang-Pauli-Str. 27, 8093 Zurich, Switzerland

²National Centre of Competence in Research PlanetS (www.nccr-planets.ch)

³Blue Marble Space Institute of Science, Seattle, WA, USA

⁴SETI Institute, 189 N. Bernardo Ave, Mountain View, CA 94043, USA

⁵ETH Zurich, Department of Earth and Planetary Sciences, Sonneggstrasse 5, 8092 Zurich, Switzerland

⁶ETH Zurich, Institute of Geochemistry and Petrology, Department of Earth and Planetary Sciences, Clausiusstrasse 25, 8092 Zurich, Switzerland

⁷NASA Postdoctoral Program Fellow, NASA Goddard Space Flight Center, 8800 Goddard Rd, Greenbelt, 20771, MD, USA

⁸European Southern Observatory, Karl-Schwarzschild-Straße 2, 85748 Garching, Germany

ABSTRACT

Identifying key observables is essential for enhancing our knowledge of exoplanet habitability and biospheres, as well as improving future mission capabilities. While currently challenging, future observatories such as the Large Interferometer for Exoplanets (LIFE) will enable atmospheric observations of a diverse sample of temperate terrestrial worlds. Using thermal emission spectra that represent conventional predictions of atmospheric CO₂ variability across the Habitable Zone (HZ), we assess the ability of the LIFE mission - as a specific concept for a future space-based interferometer - to detect CO₂ trends indicative of the carbonate-silicate (Cb-Si) weathering feedback, a well-known habitability marker and potential biological tracer. Therefore, we explore the feasibility of differentiating between CO₂ trends in biotic and abiotic planet populations. We create synthetic exoplanet populations based on geochemistry-climate predictions and perform retrievals on simulated thermal emission observations. The results demonstrate the robust detection of population-level CO₂ trends in both biotic and abiotic scenarios for population sizes as small as 30 Exo-Earth Candidates (EECs) and the lowest assessed spectrum quality in terms of signal-to-noise ratio, $S/N = 10$, and spectral resolution, $R = 50$. However, biased CO₂ partial pressure constraints hinder accurate differentiation between biotic and abiotic trends. If these biases were corrected, accurate differentiation could be achieved for populations with ≥ 100 EECs. We conclude that LIFE can effectively enable population-level characterization of temperate terrestrial atmospheres and detect Cb-Si cycle driven CO₂ trends as habitability indicators. Nevertheless, the identified biases underscore the importance of testing atmospheric characterization performance against the broad diversity expected for planetary populations.

Keywords: Habitable zone (696), Exoplanet atmospheres (487), Biosignatures (2018), Exoplanet atmospheric variability (2020), Infrared spectroscopy (2285), Space telescopes (1547)

1. INTRODUCTION

Within just a few decades, the search for potentially habitable and inhabited exoplanets has evolved from science fiction to a central scientific pursuit for the exo-

planet community. Recent advancements, from transit surveys such as the Kepler mission (Borucki et al. 2010) and the Transiting Exoplanet Survey Satellite (TESS, Ricker et al. 2015) to the launch of the James Webb Space telescope (JWST, Gardner et al. 2023), have shifted focus from exoplanet detection to characterization. However, even with JWST, characterizing temperate terrestrial exoplanet atmospheres remains chal-

lenging and time-intensive (e.g. Morley et al. 2017; Krissansen-Totton et al. 2018; TRAPPIST-1 JWST Community Initiative et al. 2024).

In the near future, ground-based observatories such as the extremely large telescopes (ELTs) have the potential to provide further data on the closest terrestrial exoplanets in reflected stellar light and thermal emission (e.g. Quanz et al. 2015; Bowens, R. et al. 2021; Kasper et al. 2021). Still, comprehensive atmospheric characterization of a significant population of these objects remains elusive, even with current and under-construction observatories. This limitation has spurred the development of next-generation mission concepts like the Habitable Worlds Observatory (HWO) and the Large Interferometer for Exoplanets (LIFE), aimed at deciphering temperate terrestrial atmospheres for habitability and biological activity indicators in reflected light and thermal emission, respectively (National Academies of Sciences, and Medicine, Engineering 2021; Miller et al. 2024; Kammerer & Quanz 2018; Quanz et al. 2022a,b). As we prepare for these future missions, the task of ensuring that their designs are able to reliably perform these characterizations is one that requires action now.

Numerous potential signatures indicative of surface oceans and global biospheres have been proposed (e.g. Meadows 2008; Kaltenegger et al. 2010; Grenfell 2017; Schwieterman et al. 2018; Schwieterman & Leung 2024). While individual planet characterization typically requires extensive contextual evidence, future missions like LIFE will enable the characterization of temperate terrestrial atmospheres on a statistically relevant sample. This capability raises the question of what we might learn about planetary habitability and biospheres by constraining planetary and atmospheric parameters on a broader scale.

One potential answer lies in the well-established concept of the Habitable Zone (HZ, Kasting et al. 1993; Kopparapu et al. 2013, 2014). The HZ describes an orbital range around a host star where temperature conditions could allow for liquid water on a terrestrial planetary surface. In the conservative HZ definition, a H₂O-CO₂ greenhouse sustains liquid surface water on an Earth-like planet due to the climate-mediating effect of the carbonate-silicate (Cb-Si) cycle (Kasting et al. 1993). On Earth, atmospheric CO₂ is linked to surface temperature by the Cb-Si weathering feedback, hypothesized to have stabilized the Earth’s climate over geological timescales (Walker et al. 1981; Sagan & Mullen 1972; Tajika & Matsui 1992; Tajika & Matsui 1993).

Translating this thermostat concept to a population of HZ planets residing at different orbital distances leads to an expected decreasing trend in atmospheric CO₂ with

increasing incident stellar flux (Kasting et al. 1993; Kopparapu et al. 2013; Kadoya & Tajika 2014; Graham & Pierrehumbert 2020). Detecting the predicted trend in atmospheric CO₂ abundance with incident stellar flux provides a unique observable directly linked to the long-term presence of liquid surface water, a fundamental prerequisite for the Cb-Si cycle to function (Walker et al. 1981; Kasting et al. 1993). Moreover, it is commonly acknowledged that biological factors, particularly land plants, influence the Cb-Si cycle by enhancing silicate weathering (Arthur & Fahey 1993; Moulton 2000; Ibarra et al. 2019; Porder 2019; Dahl & Arens 2020). By assessing the ability to distinguish between CO₂ trends on worlds hosting large-scale biospheres and abiotic planet populations, we explore the observational feasibility of CO₂ trends as population-level clues for global biotic activity.

Previous studies investigated the feasibility of observing atmospheric CO₂ abundances to infer population-level trends. As a proof of concept, Bean et al. (2017) utilized an idealized artificial planet population to propose that a decreasing CO₂ trend with incident stellar flux could be identified in a sample of 20 exoplanets, assuming ± 0.5 dex uncertainty in CO₂ abundance. The weathering feedback was only implicitly included by fixing the surface temperature over the HZ stellar irradiation range. Lehmer et al. (2020) employed a more complex coupled geochemical-climate model, confirming a decreasing trend of CO₂ abundance with incident flux but demonstrating considerable scatter. They suggested that a sample of 83 planets would be required to detect the Cb-Si distribution, excluding observational uncertainties. Further investigations by Checlair (2021) estimated that 17-34 planets would be necessary to detect the weathering feedback, incorporating simplified observational uncertainty estimates for the HabEx (Gaudi et al. 2020) and LUVOIR (Peterson et al. 2017; The LUVOIR Team 2019) mission concepts, though without a comprehensive geochemical model. More recently, Lustig-Yaeger et al. (2022) introduced a Hierarchical Bayesian Atmospheric Retrieval (HBAR) framework for hypothesis testing on predicted population-scale atmospheric trends. The authors validated their model by simulating JWST transmission spectra of a synthetic population of TRAPPIST-1e-like planets, which followed the theoretical CO₂ trend proposed by Bean et al. (2017). The authors were able to reject the null hypothesis, represented by a flat trend, as well as other simple atmospheric trend models at high confidence but acknowledged the challenge of resolving varying abundances of CO₂ with JWST-like observations.

Beyond CO₂ trends, other studies have explored the detectability of population-level signatures in synthetic exoplanet populations. The Bioverse framework, for example, combined survey simulations with Bayesian hypothesis testing to evaluate whether future transit and direct imaging missions could constrain statistical relationships, such as a correlation between planet age and atmospheric O₂ abundance or a discontinuity in planetary radii at the inner edge of the HZ (Bixel & Apai 2021; Schlecker et al. 2024). These studies, albeit focused on different observables, emphasized the importance of assessing mission concepts in terms of their ability to recover statistical trends across planetary populations.

This present study explores how population-level trends in atmospheric CO₂ abundance as a function of stellar irradiation can be robustly detected, as well as biotic and abiotic trends accurately differentiated, based on thermal emission spectra of temperate terrestrial exoplanet populations. We employ a comprehensive approach that combines detection yield simulations for a mid-infrared nulling interferometer, exemplified by the planned LIFE mission, self-consistent climate modeling throughout the HZ, and predictions for broad Cb-Si distributions based on geochemical-climate modeling results presented in Lehmer et al. (2020). We perform atmospheric retrievals on a variety of emission spectra and implement a trend inference routine following the HBAR approach as reported in Lustig-Yaeger et al. (2022).

Our framework for creating synthetic survey populations is presented in Section 2, followed by population-level atmospheric retrievals and trend analyses in Section 3. Section 4 further explores the diagnostic potential of trend detection and differentiation, highlighting identified characterization biases and their impact on trend detection capabilities. Finally, we summarize our findings and offer insights into future research directions in Section 5.

2. SYNTHETIC SURVEY AND TREND INFERENCE METHODS

Synthetic exoplanet survey populations represent the foundation of our CO₂ trend detection and differentiation analysis. To assess trend detection capabilities, the following three parameters need to be specified for each observational target:

- S : incident flux received at the planet (Section 2.1)
- $p\text{CO}_2$: atmospheric CO₂ partial pressure (Section 2.2)

- $\delta p\text{CO}_2$: observational uncertainty around a true $p\text{CO}_2$ (Section 2.3)

In the subsequent sections, we detail the process of assigning specific parameters to each planet within our synthetic survey samples. These survey populations then function as input to our trend inference routine (Section 2.4), ultimately allowing us to assess detection capabilities. To provide a clear overview of this study’s analytical steps, we have included a visual representation of our methodology in Figure 1.

2.1. Incident Flux

To set up synthetic atmospheric populations which reflect a Cb-Si-driven correlation between CO₂ abundance and stellar irradiation, we need to associate each planet with a level of incident flux S , which is characteristic for observable temperate terrestrial exoplanets residing in the HZ. This considers not only the underlying distribution of exoplanets across the HZ but also the observational biases that influence the perceived distribution.

For this, we use a two-step process: First, we generate underlying exoplanet populations based on occurrence rate estimates from Bryson et al. (2021) using the population synthesis tool P-Pop (Kammerer & Quanz 2018). Second, the mission simulator LIFESIM (Dannert et al. 2022) is used to estimate the integration time required to detect each planet within the synthetic populations, providing us with a LIFE-characteristic HZ detection yield distribution. We outline the most important aspects of both steps in the following and refer to the original publications for further details (Kammerer & Quanz 2018; Dannert et al. 2022).

To generate the underlying exoplanet population, we select FGK-type stars (3940-7220 K effective temperature) within 20 pc of the Sun from the LIFE target catalog (Quanz et al. 2022b; Menti et al. 2024). With this, we aim to produce planet populations which remain close to an Earth-Sun-like environment. Each system is assigned an exozodiacal dust level from the nominal exozodi level distribution with a median of ~ 3 zodi (Ertel et al. 2018; Ertel et al. 2020). For each star in our target sample, we generate 1000 synthetic planet populations. The large number of Monte Carlo simulations enables marginalization over population properties, reflecting uncertainties in the occurrence rate model. The underlying planet population which we present here was generated by Kammerer et al. (2022) and further analyzed in Angerhausen et al. (2024). Additional details can be found in the respective publications. The total underlying population is visualized as dotted contours in Figure 2.

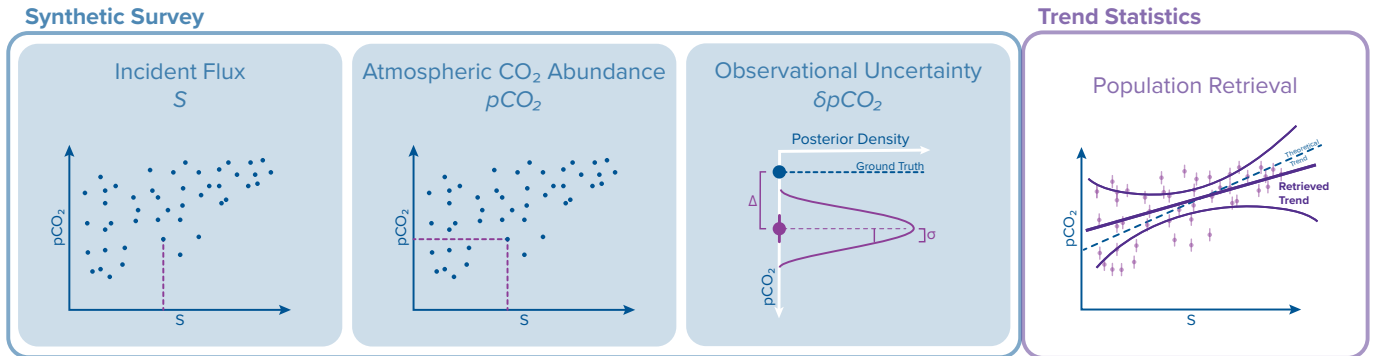


Figure 1. Schematic of our trend survey and inference methodology. We generate synthetic atmospheric populations by associating each planet with an incident flux S , injecting the predicted Cb-Si cycle-driven $p\text{CO}_2$ variability across the HZ, and assigning observational uncertainties $\delta p\text{CO}_2$. These populations then serve as input for the trend retrieval routine.

To produce the HZ detection yield population, LIFESIM estimates the integration time required to detect each planet, optimizing the distribution of observational time for habitable zone planets. Here, we limit survey populations to exo-Earth candidates (EECs), the most conservative HZ planet category (see Figure 2 for EEC bounds after Kopparapu et al. 2014; Stark et al. 2019; Quanz et al. 2022b). We simulate photon noise from stellar leakage and zodiacal dust emission. Similar to previous studies (e.g. Dannert et al. 2022; Kammerer et al. 2022; Angerhausen et al. 2024), we assume a conservatively high S/N of 7 integrated over the full LIFE-wavelength range for detection, partially to account for omitted instrumental noise. Future LIFESIM implementations will incorporate a comprehensive treatment of instrumental noise (Huber et al. 2024; Huber et al., in prep.; Dannert et al., in prep.). For each target star, we optimize the interferometer’s baseline length to maximize transmission for objects located at the HZ center. We assume LIFE mission parameters of 2 m aperture size, 5% system throughput and 4-18.5 μm wavelength coverage (Konrad et al. 2022). Other specifications correspond to those outlined in Quanz et al. (2022b). The derived EEC distribution is visualized as solid contours in Figure 2.

We show the estimated distribution of detected EECs as well as the total underlying exoplanet population in the form of radius-flux distributions in Figure 2. We observe a tendency to detect EECs toward the upper planetary radius limit, with a slight bias toward detecting planets in the outer incident flux range compared to the inner range. Comparing the derived yield distribution to the underlying population, we observe a detection bias toward larger radii, associated with enhanced thermal emission. We also note a detection preference for lower incident fluxes, which correlates with the maximum of the underlying population being located at the lower incident flux bound. Despite this, the derived yield

distribution spans the entire incident flux range, providing broad access to survey planets in our trend detection context. When comparing these results to modified mission implementations (such as varying aperture diameters), we do not observe significant changes in the incident flux distribution. While the derived EEC yield distribution corresponds to exoplanets orbiting FGK-type stars, Figure 2 includes Sun-like EEC bounds for reference. In subsequent stages of our synthetic survey setup, we constrain our analysis to Sun-like stellar irradiation bounds. However, this results in only a minor reduction in the accessible incident flux range, as $\sim 90\%$ of the detected EECs around FGK-type stars fall within these limits.

2.2. Atmospheric CO_2 Abundance

To inject the theoretically predicted $p\text{CO}_2$ - S trend into our synthetic HZ planet populations, we use the coupled geochemistry-climate model introduced by Lehmer et al. (2020). The authors applied the Cb-Si weathering framework reported in Krissansen-Totton & Catling (2017) and Krissansen-Totton et al. (2018) to a population of Earth-like planets within Sun-like EEC incident flux bounds. Lehmer et al. (2020) assumed broad variations of parameters that influence the chemical weathering process, such as weathering rates, CO_2 outgassing, and land fractions. Their results show a considerably scattered 2D $p\text{CO}_2$ - S distribution following a decreasing semi-logarithmic trend of CO_2 partial pressure with increasing incident flux. The left panel of Figure 3 shows a recreation of the 2D $p\text{CO}_2$ - S distribution from Lehmer et al. (2020). For this, we use the authors’ supplementary software (Lehmer et al. 2020) and assume parameter ranges which are identical to those used in Lehmer et al. (2020).

On Earth, land plants contribute to the Cb-Si cycle by enhancing chemical weathering and increasing atmospheric CO_2 drawdown (e.g., Dahl & Arens 2020).

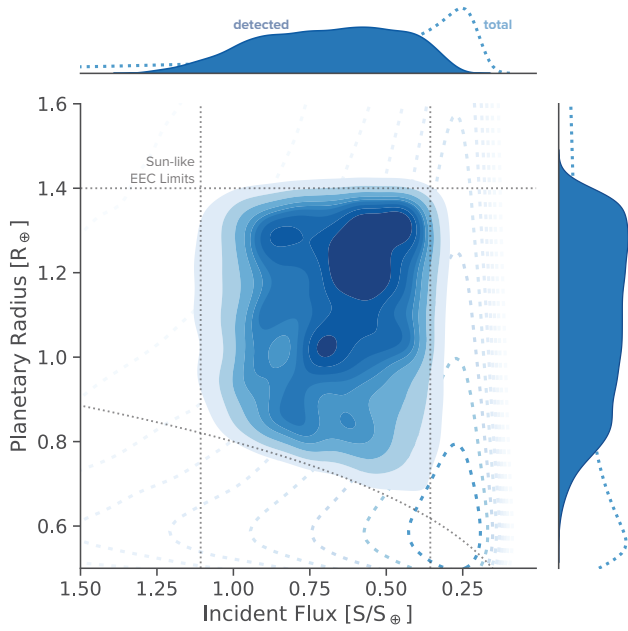


Figure 2. Distribution of simulated EEC yield (solid contours) and underlying planet population (dotted contours) around FGK-type stars within 20 pc. We show the planetary radius over incident flux distribution, where the color shading represents the relative density of planet occurrences in this parameter space. The colored contours enclose 10% to 100% of the total planet counts, with the innermost contour indicating the highest-density regions. Grey dashed lines represent EEC boundaries around a Sun-like star with $S/S_{\oplus} \in [0.356, 1.107]$ and $R/R_{\oplus} \in [0.8 \cdot S^{0.25}, 1.4]$ (Kopparapu et al. 2014; Stark et al. 2019; Quanz et al. 2022b). Top and right margin plots show the individual distributions of incident flux and planetary radius of detected and total underlying populations. Underlying synthetic planet populations are based on Kammerer et al. (2022).

Lehmer et al. (2020) broadly parameterized biological weathering by uniformly sampling the biological weathering fraction (f_{bio}) over a range of 0.1 to 1.0, representing Archean and modern Earth weathering rates, respectively. The $p\text{CO}_2$ - S distribution, referred to as biotic in this context, covers the parameter range introduced by Lehmer et al. (2020) and accounts for the assumed variability of biotically enhanced weathering rates from the early to the modern day Earth.

For this study, we additionally investigate the impact of a reduced biotic influence on the Cb-Si weathering feedback and the corresponding 2D $p\text{CO}_2$ - S distribution. We limit the biological weathering fraction parameter range in the Cb-Si cycle model to $f_{bio} = [0.1, 0.25]$, representing predominantly abiotic, non-vegetated conditions. This reduction by a factor of four is based on observational studies comparing chemical weathering fluxes on vegetated versus non-vegetated stream

catchments (Arthur & Fahey 1993; Moulton 2000). A similar modification to the Cb-Si weathering model introduced in Krissansen-Totton & Catling (2017) and Krissansen-Totton et al. (2018) was made by Hao et al. (2020) to model the absence of vegetation in the Archean Earth. The reduced atmospheric CO₂ drawdown shifts the abiotic $p\text{CO}_2$ - S distribution toward larger CO₂ partial pressures and higher surface temperatures (Figure 3, right panel). We use these predictions of biotic and abiotic distributions to associate planets in our synthetic survey population with incident flux-dependent CO₂ partial pressures.

2.3. Observational Uncertainty

In the final step of our synthetic survey setup, we assign an observational uncertainty ($\delta p\text{CO}_2$) to each simulated planet, representing the error in constraining true atmospheric CO₂ partial pressures. Preliminary hypothesis tests, detailed in Appendix A, employed a simplified model of observational uncertainty, assuming uniform uncertainty across survey populations. These initial tests demonstrated that our ability to detect and differentiate trends is significantly influenced by the magnitude of observational uncertainty on $p\text{CO}_2$.

For our primary trend detection analysis, we implement a more sophisticated approach to observational uncertainties, evaluating potential correlations between the constraints on retrieved $p\text{CO}_2$ and a planet’s position in the 2D $p\text{CO}_2$ - S parameter space. We perform atmospheric retrievals on 12 atmospheric model scenarios representing characteristic, Cb-Si cycle injected, climates throughout the HZ. This approach provides more representative $\delta p\text{CO}_2$ estimates for population-scale atmospheric diversity and enables direct translation of trend detection criteria to observational parameters such as signal-to-noise ratio, S/N , and spectral resolution, R .

We generate self-consistent atmospheric compositions using ATMOS (Arney et al. 2016, 2017) and use petitRADTRANS (Mollière et al. 2019, 2020; Alei et al. 2022) to generate atmospheric mid-infrared spectra. We then simulate observations with the LIFESIM tool and perform atmospheric retrievals using the framework introduced by Konrad et al. (2022) and updated by Alei et al. (2022) and Konrad et al. (2023). This framework uses petitRADTRANS as a forward model and pyMultiNest (Buchner 2016) for parameter inference. Subsequent sections outline our approach to constructing atmospheric scenarios, generating simulated LIFE observations, and implementing the retrieval framework.

2.3.1. Atmospheric Model Grid

We create 12 self-consistent climate scenarios that represent the predicted variability of atmospheric $p\text{CO}_2$ on

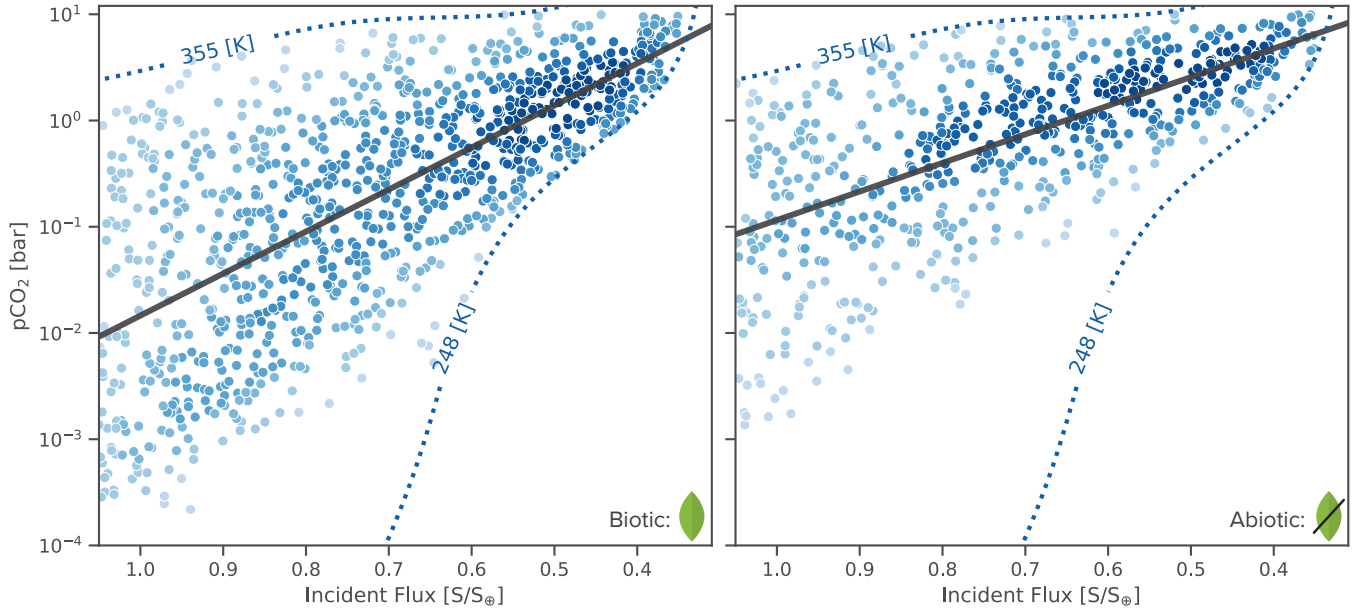


Figure 3. 2D $p\text{CO}_2$ - S distributions using coupled climate and Cb-Si cycle models (Krissansen-Totton & Catling 2017; Krissansen-Totton et al. 2018; Lehmer et al. 2020). Left panel: Biotic distribution reproducing Lehmer et al. (2020). Right panel: Abiotic distribution showing a limited biosphere contribution to the Cb-Si weathering feedback. Black lines represent weighted least squares (WLS) trend fits, yielding $\beta_{\text{bio}} = 3.96 \pm 0.18$ (95%) and $\beta_{\text{abio}} = 2.69 \pm 0.14$ (95%) with unit $-\log_{10}(p\text{CO}_2[\text{bar}])/(S/S_{\oplus})$ for biotic and abiotic trend slopes, respectively. Our β_{bio} slightly differs from Lehmer et al. (2020) due to correction for heteroskedasticity in the $p\text{CO}_2$ - S distribution. The color gradient represents the density of data points. Temperature contours indicate surface temperature limits for stable liquid water on an Earth-like planet (Charnay et al. 2013; Wolf et al. 2017).

Cb-Si planets within the HZ. For this purpose, we construct a grid in $p\text{CO}_2$ - S space, encompassing the entire parameter range of the underlying planet population produced by Lehmer et al. (2020). We model atmospheres with $p\text{CO}_2 = [10^{-4}, 10^{-3}, 10^{-2}, 10^{-1}, 1, 10]$ bar which reside at $S = [0.4, 0.7, 1.0] S_{\oplus}$ respectively. This discrete grid facilitates systematic comparison across various atmospheric scenarios. The atmospheric grid structure is visualized in Figure 4. The ModernEarth CLIMA template (Arney et al. 2016, 2017) serves as basis and is adapted according to the respective grid scenarios. In line with typical HZ climate simulations, our atmospheric compositions incorporate, besides CO_2 , H_2O as a primary greenhouse gas and N_2 as a filler species. We assume constant CO_2 volume mixing ratio (VMR) profiles. Pressure-dependent water vapor profiles are modeled self-consistently across the HZ within the CLIMA framework. For H_2O , we employ the Manabe-Wetherald parametrization, featuring empirical tropospheric water vapor and constant stratospheric water content (Manabe & Wetherald 1967). N_2 fills the remaining atmosphere such that the VMR in each atmospheric layer sums to unity. For scenarios with $p\text{CO}_2 \leq 1$ bar, we set the initial dry surface pressure to 1 bar, while for $p\text{CO}_2 = 10$ bar scenarios, it is set

to 10 bar. Figure 4 shows all generated abundance and pressure-temperature ($P-T$) profiles.

2.3.2. Simulated LIFE Spectra

To generate noisy emission spectra that are representative of observations performed with LIFE, we follow a two-step approach: First, we generate mid-infrared emission spectra for every scenario in our atmospheric grid using the 1D plane-parallel radiative transfer code *petitRADTRANS* (Mollière et al. 2019, 2020; Alei et al. 2022). Second, we estimate the observational noise with the mission simulator tool LIFESIM (Dannert et al. 2022). While we use LIFE as specific mission concept, the subsequent analyses are based on defined spectrum quality metrics, such as S/N and R , which are broadly applicable to comparable mission concepts.

We consider two signal-to-noise ratios $S/N = [10, 20]$ and two spectral resolutions $R = [50, 100]$ for all 12 spectra, based on preliminary LIFE requirements (Konrad et al. 2022, 2023; Alei et al. 2022). R is defined as $\lambda/\Delta\lambda$, where λ is the wavelength at the bin center and $\Delta\lambda$ denotes the bin width. Input for the radiative transfer routine includes pressure-dependent species profiles and $P-T$ profiles from the previous step (Section 2.3.1). We use HITRAN 2020 (HN20; Gordon et al. 2022) opacity line lists and account for collision-induced absorption (CIA) and Rayleigh scattering for all species (Table 1).

Table 1. Line and continuum opacities.

Molecular Line Opacities				CIA		Rayleigh Scattering	
Molecule	Line List	Pressure Broadening	Wing cutoff	Pair	Reference	Molecule	Reference
CO ₂	HN20	γ_{air}	25 cm ⁻¹	N ₂ -N ₂	Karman et al. (2019)	N ₂	Thalman et al. (2014, 2017)
H ₂ O	HN20	γ_{air}	25 cm ⁻¹	CO ₂ -CO ₂	Karman et al. (2019)	CO ₂	Sneep & Ubachs (2005)
N ₂	HN20	γ_{air}	25 cm ⁻¹	H ₂ O-H ₂ O	Karman et al. (2019)	H ₂ O	Harvey et al. (1998)
				H ₂ O-N ₂	Karman et al. (2019)		

Table 2. Parameters of forward model and assumed priors in the retrieval.

Parameter	Description	Prior
a_4	P - T parameter	$\mathcal{U}(-10,10)$
a_3	P - T parameter	$\mathcal{U}(-50,50)$
a_2	P - T parameter	$\mathcal{U}(-100,500)$
a_1	P - T parameter	$\mathcal{U}(0,500)$
a_0	P - T parameter	$\mathcal{U}(0,1000)$
$\log_{10}(P_0)$	\log_{10} (Surface pressure [bar])	$\mathcal{U}(-4,3)$
R_{pl}	Planet radius [R_{\oplus}]	$\mathcal{G}(1.0,0.2)$
$\log_{10}(M_{pl})$	\log_{10} (Planet mass [M_{\oplus}])	$\mathcal{G}(0.0,0.4)$
$\log_{10}(\text{CO}_2)$	\log_{10} (CO ₂ mass fraction)	$\mathcal{U}(-15,0)^*$
$\log_{10}(\text{H}_2\text{O})$	\log_{10} (H ₂ O mass fraction)	$\mathcal{U}(-15,0)$
$\log_{10}(\text{N}_2)$	\log_{10} (N ₂ mass fraction)	$\mathcal{U}(-15,0)$

NOTE— $\mathcal{U}(x,y)$ indicates a uniform prior with a lower limit x and upper limit y . $\mathcal{G}(\mu,\sigma)$ denotes a Gaussian prior with mean μ and standard deviation σ . *For $p\text{CO}_2 \geq 1$ bar cases, we apply uniform priors $\mathcal{U}(0,1)$ on the CO₂ mass fraction.

Cloud effects are omitted in our atmospheric models, with implications discussed in Section 4.3. We assume that all planets in our grid are at a 10 pc system distance, orbiting a G2V star.

LIFESIM estimates wavelength-dependent noise to simulate LIFE observations of the spectrum population. Following previous analyses (e.g. Konrad et al. 2022, 2023; Alei et al. 2022), we define the S/N of the spectrum as the S/N in a reference wavelength bin. Here, we choose a reference bin at 11.5 μm , which is undisturbed by strong absorption features in our emission spectrum population. The S/N at all other wavelengths is then determined by the LIFESIM noise model, which accounts for photon noise by the planet as well as major astrophysical noise sources. We do not randomize spectral points based on S/N , but understand S/N as uncertainty around the true spectral points. Implications of this choice are discussed in detail in Konrad et al. (2022).

Figure 4 displays the resulting modeled noisy emission spectra of our 12 atmospheric scenarios.

2.3.3. Bayesian Atmospheric Retrieval Framework

With the help of atmospheric retrievals, observations of noisy spectra can be translated to estimates of planetary and atmospheric parameters. Retrieval routines typically consist of two components - a forward model and a parameter inference algorithm. The former infers atmospheric spectra on the basis of planetary and atmospheric parameters. The latter then searches the prior space that is defined by prior beliefs, prior probability distributions (priors), which we choose for the model parameters, and finds the parameter combinations that best fit the noisy spectrum we used as input to the retrieval. All possible parameter combinations are then provided in form of posterior probability distributions (posteriors) (for a review, see, e.g., Madhusudhan 2018).

Similar to the generation of our input spectra, we use `petitRADTRANS` to calculate theoretical 1D mid-infrared emission spectra as forward model in the retrieval. As parameter inference model we use `pyMultiNest` (Buchner 2016), a Python interface for the `MultiNest` nested sampling package (Feroz et al. 2009). All retrievals were run with 600 live points and a sampling efficiency of 0.3, which is recommended for evidence evaluation.

In the retrieval forward model we parameterize the $P - T$ profile with a fourth-order polynomial

$$T(P) = \sum_{i=0}^4 a_i \log_{10}(P^i). \quad (1)$$

Here, P represents pressure, T the respective temperature and a_i the parameters of the $P - T$ model. We choose a polynomial $P - T$ model in order to allow for a broad description of thermal structures, which is required in the context of analyzing a broad variety of atmospheric states within our atmospheric grid. We use the same line lists as in the input spectra and take into account CIA and Rayleigh scattering (see Table 1). This choice is motivated by systematic biases that can be introduced to the retrieval when different sets of opacities

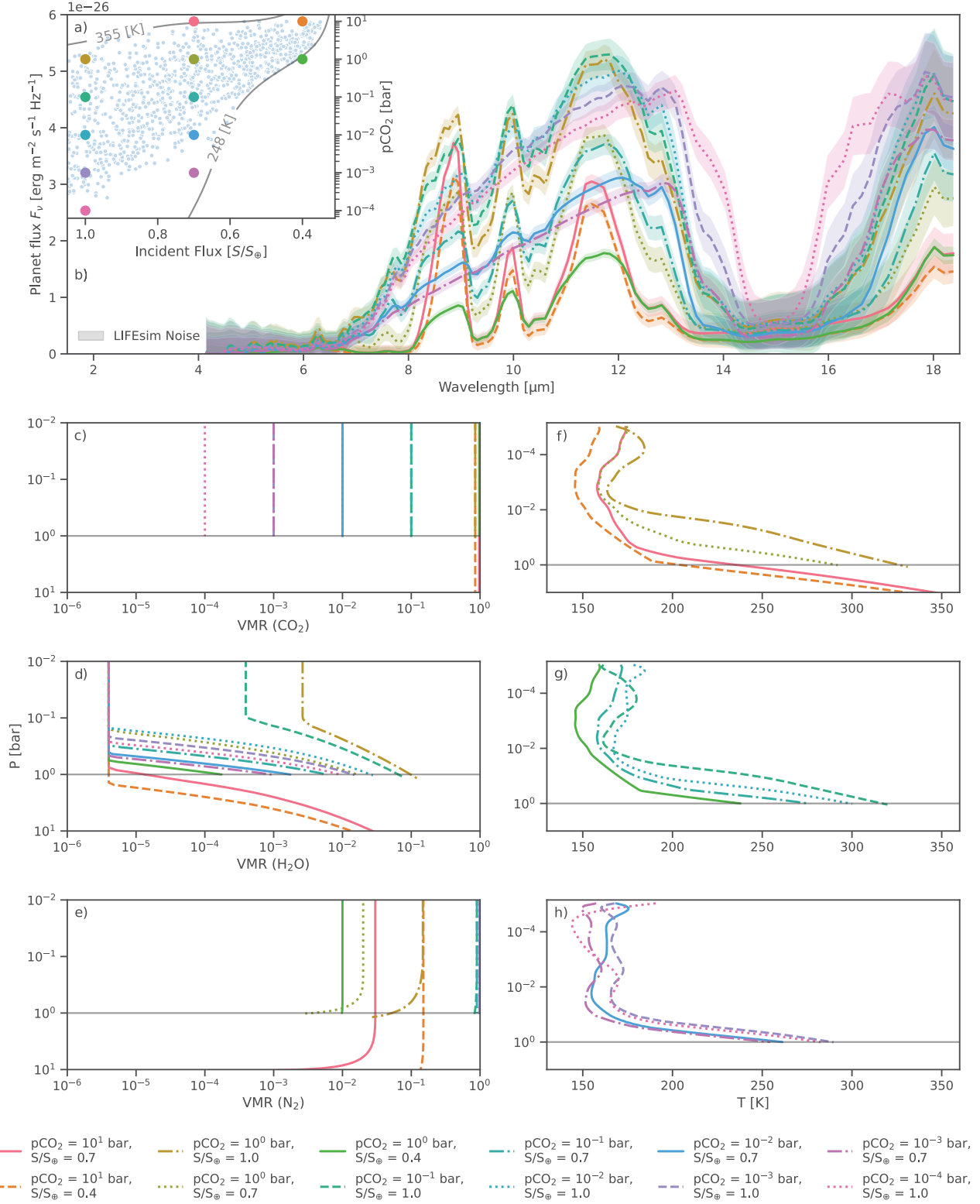


Figure 4. Atmospheric profiles and emission spectra for the 12 atmospheric scenarios covered by our grid. (a) Atmospheric grid structure visualization. (b) Simulated emission spectra with LIFESIM noise estimates for $S/N = 20$ and $R = 100$. (c)-(e) VMR profiles for CO_2 , H_2O , and N_2 . (f)-(h) $P - T$ profiles grouped into three sets of four atmospheric scenarios each, to facilitate visualization. Color-coding in all panels corresponds to individual scenarios within the population.

are used in the input spectra and the retrieval forward model. For further discussions on this we refer to [Alej et al. \(2022\)](#). We assume constant abundance profiles for all atmospheric species and omit the effect of clouds in our retrieval framework. Implications of these simplifications are discussed in Section 4.3.

The priors we select for our model parameters are listed in Table 2. The priors on the $P - T$ profile parameters a_i and the surface pressure P_0 are chosen to cover a wide range of thermal structures. We choose broad uniform prior ranges on the \log_{10} mass fraction for all species. In case of the $\text{pCO}_2 \geq 1$ bar scenarios in our atmospheric grid, we instead set a uniform prior on the mass fraction to enable an increased sampling density in the high abundance regime. This approach is justified as constraints around high CO₂ abundances are retrieved when assuming log-uniform priors on the CO₂ abundance. Such a result would naturally be followed by a retrieval inference allowing for increased sensitivity for high species abundances. Consistent with previous retrieval studies (see e.g. [Konrad et al. 2022, 2023](#); [Alej et al. 2022](#)), we use Gaussian priors for planet radius R_{pl} and mass M_{pl} . This choice is motivated by an expected constraint on R_{pl} provided by the planet detection with LIFE ([Dannert et al. 2022](#)). Given the R_{pl} prior, we can derive a prior on $\log_{10}(M_{pl})$ by using the probabilistic mass-radius relation model *Forecaster* ([Chen & Kipping 2016](#)).

2.4. Population Trend Inference Routine

To extract population-level atmospheric trends from a set of atmospheric observations and their corresponding retrieval estimates (i.e., pCO_2 posteriors), we employ a hierarchical Bayesian atmospheric retrieval (HBAR) approach. This methodology, introduced by [Lustig-Yaeger et al. \(2022\)](#), is based on the importance sampling formalism developed by [Hogg et al. \(2010\)](#). In the following, we provide a description of the most relevant aspects of the HBAR framework and refer to the original publications for further details.

We perform a Bayesian inference on the population-level CO₂ trend based on a series of simulated atmospheric observations. We introduce a set of hierarchical (hyper-) parameters γ , which characterize the trend model. We then solve the Bayesian inverse problem for these parameters. Applying Bayes theorem we obtain

$$\mathcal{P}(\gamma | \{\mathbf{D}_n\}_{n=1}^{N_P}) \propto \mathcal{L}_\gamma \mathcal{P}(\gamma), \quad (2)$$

where $\mathcal{P}(\gamma | \{\mathbf{D}_n\}_{n=1}^{N_P})$ denotes the posterior for the population parameters γ . $\mathcal{P}(\gamma)$ corresponds to the priors we set for the population parameters and \mathcal{L}_γ is the likelihood. The latter is where CO₂ abundance posteri-

ors from individual planet observations come into play. Here, \mathbf{D}_n represents a set of spectroscopic observations for each planet n in a total population of N_P exoplanets. Given the population parameters γ , the probability of the population-level dataset is then defined as

$$\mathcal{L}_\gamma \equiv \mathcal{P}(\{\mathbf{D}_n\}_{n=1}^{N_P} | \gamma). \quad (3)$$

After a set of rearrangements for which we refer to [Lustig-Yaeger et al. \(2022\)](#), we obtain the following expression

$$\mathcal{L}_\gamma \approx \prod_{n=1}^{N_P} \frac{1}{K} \sum_{k=1}^K \frac{\mathcal{P}_\gamma(f_{\text{CO}_2nk})}{\mathcal{P}_0(f_{\text{CO}_2nk})}. \quad (4)$$

Equation 4 considers K posterior samples from the original atmospheric retrieval posteriors, where k represents the sample index. $\mathcal{P}_0(f_{\text{CO}_2nk})$ denotes the original uninformative prior for CO₂ abundance used in the individual atmospheric retrievals. We introduce an updated prior probability distribution, $\mathcal{P}_\gamma(f_{\text{CO}_2nk})$, which provides a more informed prior on CO₂ abundance compared to the original uninformative priors. The posterior distributions, derived from the atmospheric retrieval grid, are implicitly included within the K samples.

Until this point, we have not specified the population parameters γ that we intend to retrieve. For this, we set up a functional form for the theoretical population-trend. Similar to [Lehmer et al. \(2020\)](#), we fit a semi-logarithmic trend to the data, modeling the partial pressure of CO₂ as a function of incident flux. The functional form follows

$$\log_{10}(\text{pCO}_2) = f_{\text{CO}_2}(\alpha, \beta) = \alpha + \beta \cdot S/S_\oplus, \quad (5)$$

where α represents the log-intercept and β corresponds to the logarithmic slope. With the trend model fixed, we give a description of the updated prior $\mathcal{P}_\gamma(f_{\text{CO}_2nk})$ which corresponds to a normal distribution that is dependent on population parameters γ

$$\mathcal{P}_\gamma(f_{\text{CO}_2nk}) = \mathcal{N}(f_{\text{CO}_2nk} - f_{\text{CO}_2}(\alpha, \beta), \sigma_N). \quad (6)$$

Here, σ_N corresponds to the standard deviation of the normal distribution, which assigns high probability to pCO_2 values of the theoretical trend lying near the retrieved pCO_2 posterior samples. Finally, we introduce our population parameters $\gamma = [\alpha, \beta, \sigma_N]$, for which we choose broad prior distributions

$$\mathcal{P}(\gamma) \begin{cases} \alpha \sim \mathcal{U}(-10, 10) \\ \beta \sim \mathcal{U}(-10, 10) \\ \sigma_N \sim \mathcal{N}_{1/2}(0, 1). \end{cases} \quad (7)$$

Following [Lustig-Yaeger et al. \(2022\)](#), we adopt the same prior for $\sigma_{\mathcal{N}}$, where $\mathcal{N}_{1/2}(0, 1)$ denotes a half-normal distribution with a mean of 0 and a standard deviation of 1. The inferred posteriors of population parameters γ will then provide us with population-level trend constraints that encode the information from individually retrieved pCO₂ posteriors.

3. TREND STATISTICS: POPULATION RETRIEVAL RESULTS

We outline our retrieval results for the simulated atmospheric grid in [Section 3.1](#), discuss the setup of posterior maps in [Section 3.2](#), and show results of the population-level trend retrievals in [Section 3.3](#).

3.1. Atmospheric Retrieval Results

We present atmospheric retrieval results for our grid of 12 atmospheric scenarios representing the predicted variability of CO₂ abundance on Cb-Si planets across the HZ. In [Figure 5](#) we show retrieved constraints on the CO₂ abundance, i.e. volume mixing ratios (VMR), for all considered spectrum quality scenarios covering $S/N = [10, 20]$ and $R = [50, 100]$. Moving forward, we use CO₂ partial pressures to distinguish between different parameter spaces within the atmospheric population. This notation is chosen because pCO₂, when combined with incident flux, serves as a unique identifier for our atmospheric scenarios, unlike CO₂ VMRs. Additionally, we make a clear distinction between abundances (expressed as VMRs) and partial pressures.

Several qualitative observations can be made from [Figure 5](#). As the true atmospheric CO₂ abundance increases, the constraints on the retrieved CO₂ abundance become tighter. Higher observational sensitivity, characterized by increased S/N and R , generally improves the precision (reduces standard deviations) of the retrieved posterior distributions. For most atmospheric scenarios and observational sensitivity cases, the CO₂ abundance is well-constrained, with the ground truth falling within the 1σ envelope of the retrieved parameter estimate. However, the accuracy (offset between ground truth and posterior median) of the constraints varies between pCO₂ ≥ 1 bar and pCO₂ < 1 bar parameter spaces.

For pCO₂ ≥ 1 bar scenarios, we additionally plot posterior distributions in non-log scale, since we chose non-log uniform priors to achieve a better sampling density for these high abundance cases. In this parameter space, we observe tight posterior constraints at the upper edge of the prior space, constraining well the ground truth CO₂ abundances for all scenarios. For the pCO₂ < 1 bar cases, we generally observe a tendency for CO₂ posteriors to be offset toward larger abundances compared to

the ground truth. For the highest observational sensitivity ($S/N = 20$, $R = 100$), the CO₂ abundance is over-estimated on average by a ~ 1 dex offset between ground truth and posterior median. With increasing true CO₂ abundance, the bias in retrieved abundance estimates becomes more significant. As a result, the ground truth does not fall within the 1σ posterior envelope for any observational sensitivity case in the pCO₂ = 10⁻¹ bar and $S/S_{\oplus} = 1.0$ scenario. Moreover, the tendency to over-estimate CO₂ abundances is visibly more pronounced for atmospheres receiving an incident flux of $S/S_{\oplus} = 1.0$ compared to $S/S_{\oplus} = 0.7$ cases.

3.2. CO₂ Posterior Maps

Our atmospheric retrieval grid provides us with a population of 12 CO₂ abundance posteriors for each spectrum quality scenario. To ensure consistency with the underlying theoretical pCO₂- S distributions and respective population trends, we translate abundance (VMR) posteriors to partial pressure posteriors via point-wise multiplication of retrieved CO₂ abundance and surface pressure, P_0 , constraints

$$\mathcal{P}(\text{pCO}_2) = \mathcal{P}(\text{VMR}(\text{CO}_2)) \cdot \mathcal{P}(P_0), \quad (8)$$

where \mathcal{P} represents the retrieved posterior. Subsequently, we generate characteristic posteriors maps for each spectrum quality scenario by interpolating between the pCO₂ posteriors obtained from the atmospheric retrieval population. These posterior maps then allow us to associate any planet in our survey populations with a pCO₂ posterior that is informed by our grid of atmospheric retrievals. For this, we fit Gaussian distributions to the derived pCO₂ posteriors and then interpolate between obtained standard deviations σ and offsets Δ (difference between posterior median and true partial pressures). In cases where the posterior distribution deviates from a well-defined Gaussian shape and instead provides only upper or lower bounds on pCO₂, resembling a Gaussian peak with non-negligible tail on one side, our analysis focuses solely on the Gaussian component, which we refer to as the sensitivity peak. Following classifications in [Konrad et al. \(2022\)](#), we denote such posteriors as sensitivity-limited (SL).

We perform a linear interpolation between grid points situated at the ground truth pCO₂ values. To achieve completeness, the maps are then expanded to cover the entire 2D pCO₂- S parameter space using nearest-neighbor interpolation. Hence, σ and Δ maps may not accurately represent parameter spaces that fall substantially outside the established grid boundaries. [Figure 6](#) visualizes obtained σ and Δ maps for the $S/N = 20$ and $R = 100$ scenario. A positive (negative) offset implies

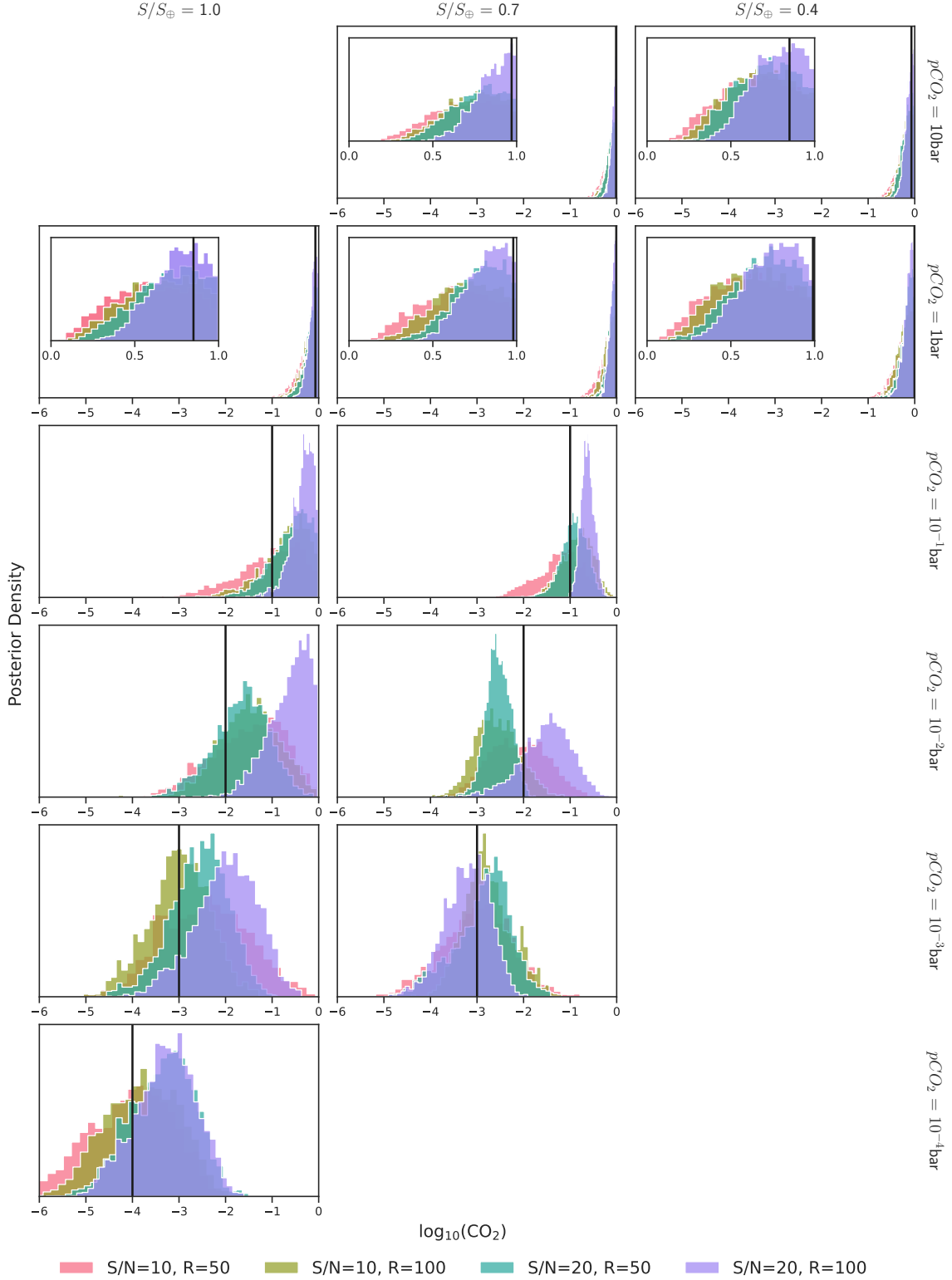


Figure 5. Posterior distributions of CO₂ abundance derived from atmospheric spectrum retrievals. The panels are arranged to reflect the atmospheric grid within the pCO₂- S parameter space. Columns represent different stellar insolation values, $S/S_{\oplus} = 1.0, 0.7, 0.4$, while rows correspond to different CO₂ partial pressures, pCO₂ = 10 bar, 1 bar, 10⁻¹ bar, 10⁻² bar, 10⁻³ bar, 10⁻⁴ bar. Each panel shows results for four combinations of signal-to-noise ratio, $S/N = [10, 20]$, and spectral resolution, $R = [50, 100]$. Thick black lines indicate the ground truth CO₂ abundance. For scenarios with pCO₂ \geq 1 bar, additional posterior distributions are plotted in non-logarithmic scale.

a shift of posteriors to higher (lower) partial pressures with respect to the true $p\text{CO}_2$. Posterior maps generated for all spectral quality cases and the full population of retrieved $p\text{CO}_2$ posteriors are shown in Appendix B.

Similar to the abundance constraints (Section 3.1), we identify wider posteriors toward low $p\text{CO}_2$ and high S/S_\oplus parameter ranges. However, we retrieve $p\text{CO}_2$ posteriors which are narrower constrained and more centered around the ground truths ($\sigma \leq 0.4$ dex, $\Delta \leq 0.75$ dex). Systematic differences between the retrieved abundance and partial pressure constraints result from multiplying posteriors of CO_2 abundance with surface pressure, two parameters that exhibit degeneracy in our retrievals. This will be discussed further in Section 4.2. For atmospheres with $p\text{CO}_2 \geq 1$ bar, we observe a trend of negative offsets in $p\text{CO}_2$ posteriors relative to ground truths. In particular, scenarios with $p\text{CO}_2 = 10$ bar are underestimated, with ground truths falling outside the 1σ posterior envelope. Conversely, in the $p\text{CO}_2 < 1$ bar range, we note a tendency for positive offsets between posterior means and true partial pressures.

3.3. Trend Retrieval Results

We draw four sets of survey populations with $N_P = [10, 30, 50, 100]$ planets. Based on the results of our preliminary hypothesis tests (see Appendix A), which estimated the necessary sample sizes for detecting and distinguishing CO_2 trends using a simplified observational uncertainty model, we choose a broad range of survey population sizes. For each population, we assign incident fluxes (Section 2.1), CO_2 partial pressures (Section 2.2), and $p\text{CO}_2$ posteriors corresponding to the respective location of the scenario in σ and Δ maps (Section 3.2).

Figure 7 displays the retrieved population-level $p\text{CO}_2$ - S trends for all N_P , encompassing both biotic and abiotic scenarios in the highest spectral quality case ($S/N = 20$, $R = 100$). The blue shaded areas indicate 1σ , 2σ , and 3σ credible intervals (CrI) of the retrieved trends. Mirroring the underlying Cb-Si distributions (Section 2.2), $p\text{CO}_2$ draws exhibit greater scatter at higher incident fluxes, particularly evident in high N_P scenarios. The abiotic survey population shows less spread compared to the biotic one, primarily occupying the $p\text{CO}_2 \geq 10^{-2}$ bar parameter space. Comparing the drawn survey populations to the underlying Cb-Si distributions (see Figure 3) reveals populations which are more compressed along the $p\text{CO}_2$ axis, reflecting the impact of offsets between associated posteriors and true $p\text{CO}_2$ values. In line with the σ map for the observational sensitivity case $S/N = 20$ and $R = 100$,

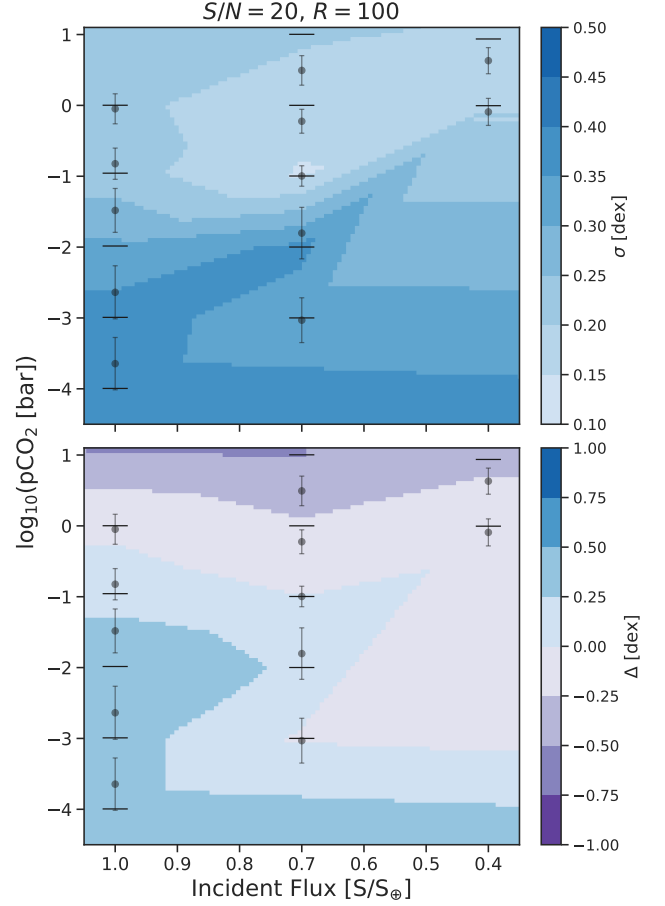


Figure 6. Maps of posterior standard deviations (σ) and offsets (Δ) for observational sensitivity case $S/N = 20$ and $R = 100$. Color shading indicates the magnitude of σ (top) and Δ (bottom), with blue and purple representing positive and negative offsets, respectively. Black horizontal lines denote ground truth CO_2 partial pressures. Data points with error bars represent median and 1σ envelope of Gaussian fits to retrieved $p\text{CO}_2$ posterior distributions.

broader posteriors of up to ~ 0.4 dex are observed for $p\text{CO}_2 < 1$ bar scenarios compared to $p\text{CO}_2 \geq 1$ bar cases.

Several general observations can be made: As expected, larger survey populations N_P result in more precise constraints on the retrieved trend slope. However, these scenarios also demonstrate a more evident deviation of the retrieved trend constraint from the injected population-level trend. These patterns are also evident in the retrieved posteriors of slope parameter β , which are displayed for all N_P and both biotic and abiotic scenarios in Figure 8. In general, the biotic scenario produces steeper trends compared to the abiotic one. The abiotic case yields more constrained slope estimates, which is consistent with a less dispersed underlying Cb-Si distribution.

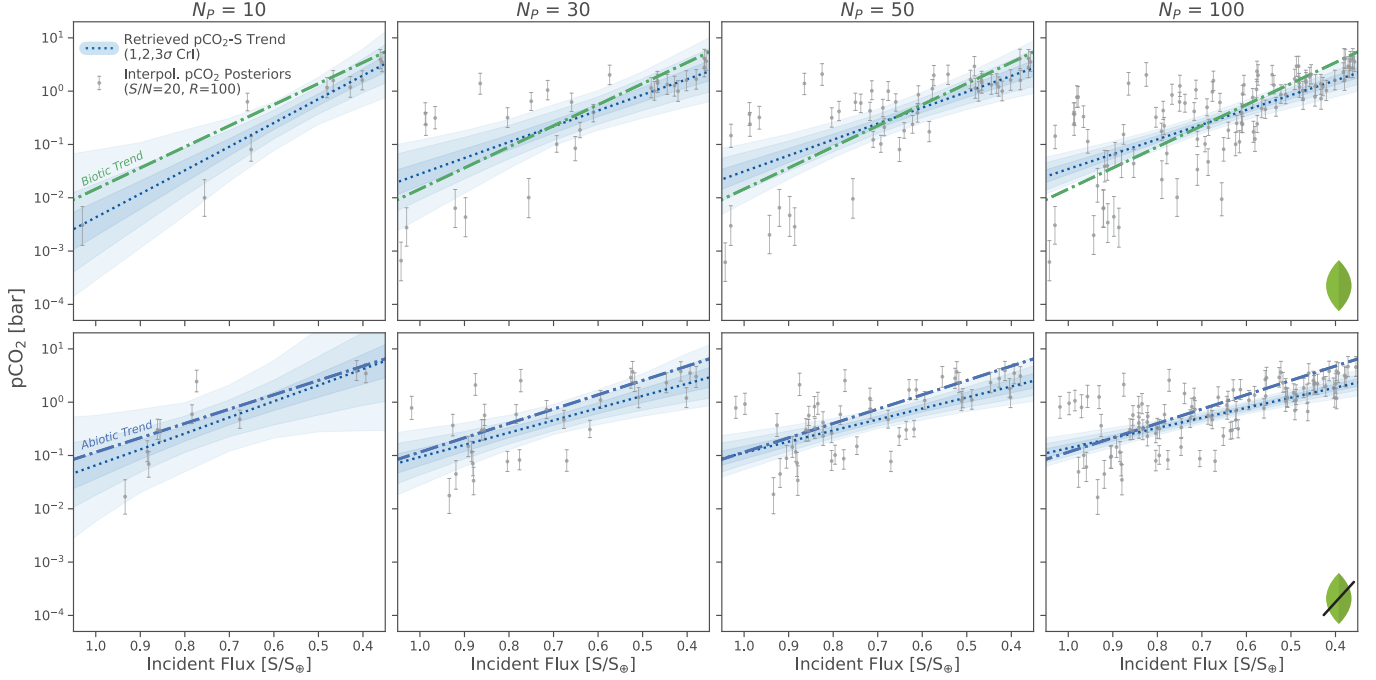


Figure 7. Retrieved population-level trends for biotic (top) and abiotic (bottom) scenarios for spectrum quality case $S/N = 20$ and $R = 100$. We differentiate between population sizes $N_P = [10, 30, 50, 100]$. Dotted blue lines indicate median retrieved trends while blue shading indicates 1σ , 2σ and 3σ CrIs. Dashed lines represent theoretical biotic (green) and abiotic (blue) CO₂ trends. Grey data points with error bars show median and 1σ envelope of pCO₂ posteriors, which correspond to a (pCO₂, S) pair's location in σ and Δ maps.

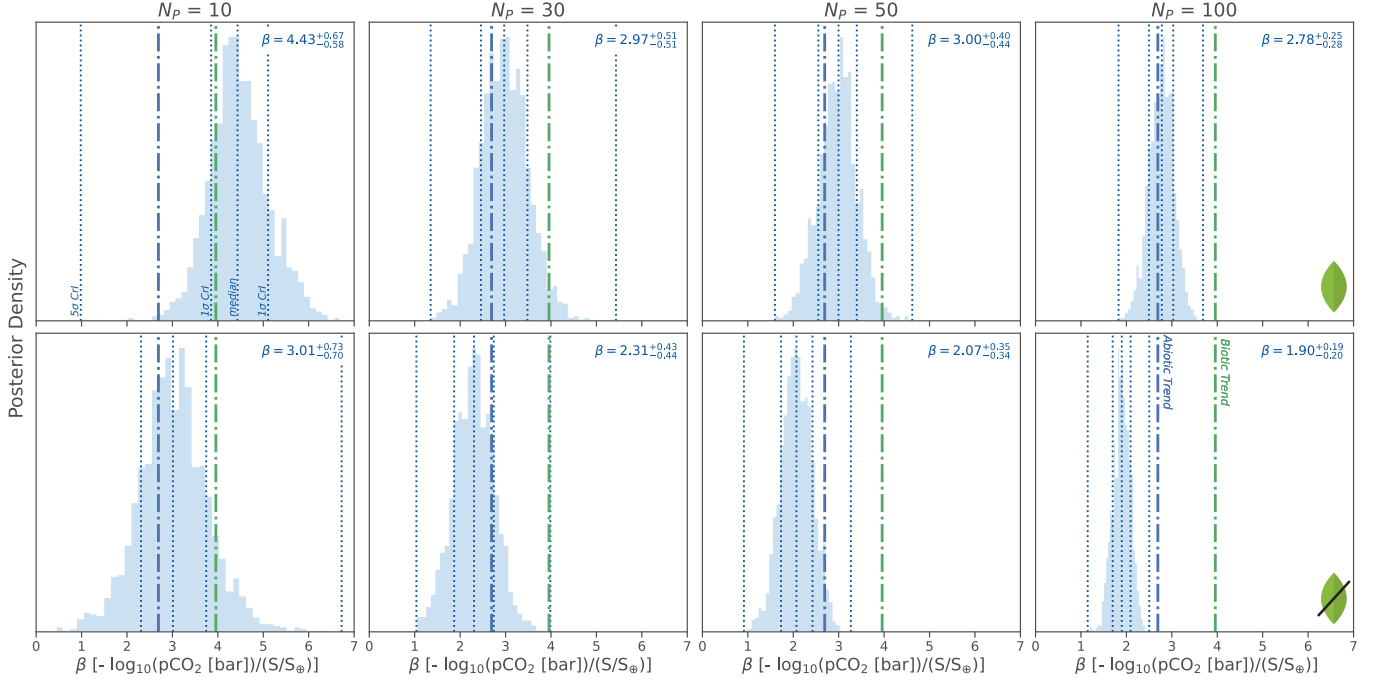


Figure 8. Retrieved posterior distributions of the slope parameter β for biotic (top) and abiotic (bottom) scenarios for spectrum quality case $S/N = 20$ and $R = 100$. We differentiate between population sizes $N_P = [10, 30, 50, 100]$. Dashed vertical lines indicate theoretical biotic (green) and abiotic (blue) CO₂ trend slopes. Dotted blue lines represent median, 1σ , and 5σ CrIs of the trend slope posterior. Median and 1σ values of the retrieved posteriors are displayed in the top right for each scenario.

For a survey population of $N_P = 10$ planets in the biotic case, the null slope ($\beta = 0$) falls beyond the 5σ CrI of the retrieved trend slope posterior, indicating that a flat trend is highly improbable given the model and data. As N_P increases to 30 or more, an even clearer distinction emerges between retrieved and flat trends for both biotic and abiotic cases. However, as already shown in Figure 7, larger N_P values lead to a more pronounced bias in trend detection, favoring flatter CO_2 trends compared to the true injected population-level trend. For $N_P = 100$, the true trend slopes lie outside the 5σ CrI of the posterior distributions. Notably, the scenario characterized by the lowest observational sensitivity ($S/N = 10$, $R = 50$) does not show significant variations in the derived trend constraints, as depicted in Appendix C.

4. DISCUSSION

In the subsequent sections, we further evaluate the detection potential of CO_2 trends in terrestrial HZ atmospheres (Section 4.1), drawing on our population-trend retrieval results, and address observational biases as well as their implications for trend detection capabilities (Section 4.2). Finally, we outline the limitations of this work in Section 4.3.

4.1. Diagnostic Potential of population-level CO_2 Trend Detection and Distinction

In Section 3.3, we inferred population-level CO_2 trends based on synthetic survey populations and conducted an initial comparison of retrieved trend estimates with ground truth (biotic and abiotic) population trends, as well as flat trends representative of a non-existent relationship between pCO_2 and the incident flux received by the planets. The following sections provide a deeper look at the detection and distinction potential of population-level CO_2 trends.

4.1.1. Detecting CO_2 Trends

To quantify the sensitivity of a CO_2 trend detection (i.e. flat trend rejection) to population size N_P and spectrum quality represented by S/N and R , we use the Bayesian evidence \mathcal{Z} . \mathcal{Z} is a model performance metric that, in this case, estimates how well the forward model fits the input trend population. By running our population-trend retrieval routine with two different trend models, a linear trend (Model A) and a flat trend (Model B, $\log_{10}(\text{pCO}_2) = f_{\text{CO}_2}(\alpha) = \alpha$), our pipeline yields different evidences dependent on the model. With these, we derive the Bayes' factor K :

$$\log_{10}(K) = \frac{\ln(\mathcal{Z}_A) - \ln(\mathcal{Z}_B)}{\ln(10)}. \quad (9)$$

The Bayes' factor indicates the preferred model. A positive $\log_{10}(K)$ indicates a preference for a linear trend (Model A) and a negative value shows a preference for a flat trend (Model B). The strength of this preference is further quantified on the basis of the Jeffreys scale (Appendix C, Jeffreys 1939).

In Figure 9, we compare the Bayes' factor K for all combinations of population size, $N_P = [10, 30, 50, 100]$, and spectrum quality, $S/N = [10, 20]$ and $R = [50, 100]$, assessed in this study. The top grid shows $\log_{10}(K)$ values for the biotic case, whereas the bottom grid indicates the abiotic scenario. In the biotic case, we see a decisive preference ($\log_{10}(K) > 2$) for the linear over the flat trend model, which we denote here as a robust trend detection, for all population sizes and spectrum quality scenarios. In the abiotic $N_P = 10$ case, we infer substantial ($0.5 < \log_{10}(K) > 1$) and strong ($1 < \log_{10}(K) > 2$) support for a linear model, in $S/N = 10$ and $S/N = 20$ cases respectively. For $N_P \geq 30$, the linear model is again decisively preferred over the flat trend model.

In summary, the linear model is consistently preferred over the flat model. For $N_P \geq 30$, a population-level CO_2 trend is robustly detected for both biotic and abiotic cases in all regarded spectrum quality scenarios. Additionally, we identify a strong sensitivity of trend preference strength to N_P , while spectrum quality metrics S/N and R play a minor role in detection confidence. Yet, here we assess the diagnostic potential of one drawn population per respective N_P scenario. Due to the wide spread of the assumed underlying Cb-Si distributions, a follow-up draw in the low N_P regime might lead to differences in precision and accuracy of the retrieved population-level trend and, hence, might impact trend detectability for the lowest N_P considered here.

4.1.2. Differentiating Biotic and Abiotic CO_2 Trends

In Section 3.3 we identified a biased retrieval of population-level trends toward flatter slopes for both biotic and abiotic cases, which become more pronounced with increasing planet population size. Here, we discuss these offsets and assess which factors play a role for precision and accuracy of our population-trend inferences.

To evaluate the sensitivity of retrieved trend constraints to various parameters, we examine four distinct model assumptions within our trend retrieval analysis framework. Figure 10 illustrates the trend slope posteriors for each model assumption scenario. In this analysis, we focus solely on the highest population size ($N_P = 100$) and the most sensitive observational case ($S/N = 20$, $R = 100$), as these conditions allow for the clearest identification of differences in trend constraints.

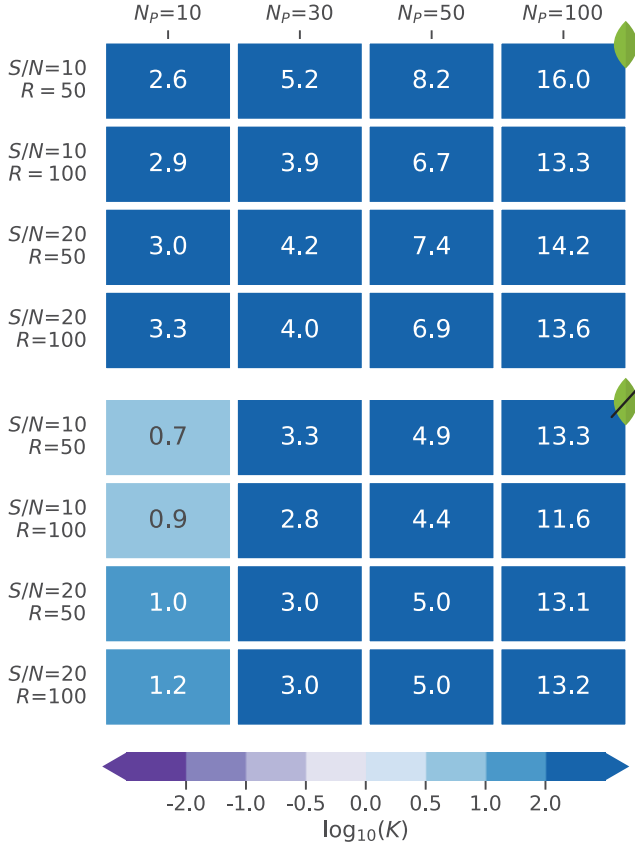


Figure 9. Bayes’ factor comparison of linear and flat trend models for biotic (top) and abiotic (bottom) scenarios and for various combinations of population size $N_P = [10, 30, 50, 100]$ and spectrum quality, $S/N = [10, 20]$ and $R = [50, 100]$. Positive $\log_{10}(K)$ values (blue) indicate a preference for the linear trend model, whereas negative $\log_{10}(K)$ values (purple) favor the flat trend model. The color intensity corresponds to the strength of preference according to the Jeffreys scale (Appendix C, Jeffreys 1939).

The model comparison involves four scenarios to assess the ability to distinguish between biotic and abiotic CO₂ trends:

- 1) Base scenario: CO₂ posterior distributions with standard deviations and offsets based on σ and Δ maps, respectively.
- 2) No offset scenario: Neglected offsets Δ between posterior means and true pCO₂, with self-consistent posterior σ for each planet.
- 3) Fixed standard deviation scenario: Neglected offsets Δ and fixed posterior standard deviation of $\sigma = 0.1$ dex for all atmospheres.
- 4) Reduced scatter scenario: Neglected offsets Δ , fixed $\sigma = 0.1$ dex, and true pCO₂ within ± 0.1 dex of the true CO₂ trend.

Our analysis of the four scenarios reveals distinct patterns in retrieved trend posteriors. In the first scenario, which corresponds to our base analysis setup, a notable shift toward flatter trends is observed for both biotic and abiotic cases. The second scenario shows trend posteriors which successfully constrain the ground truth within $\sim 1\sigma$ CrI for both cases. A slight improvement in trend constraint accuracy is evident in the third scenario. The final scenario, which mimics a population with reduced scatter in pCO₂, shows a significant increase in trend constraint precision.

The comparison indicates that the posterior offset Δ significantly affects trend constraint accuracy, whereas the precision of trend constraints is largely influenced by population scatter, in addition to the planet population size N_P as discussed in Section 3.3. This suggests that if offsets were to be corrected, an accurate trend retrieval could be achieved for a population size of $N_P \geq 100$. Although observers cannot control the inherent variability of true pCO₂ in an actual atmospheric population, future mission designs have the potential to optimize the number of planets in the population (N_P) and address biased pCO₂ estimates (Δ) derived from atmospheric retrieval frameworks.

Population sizes of this magnitude inevitably raise questions regarding feasible yields. While the LIFE mission progresses in its concept phase, previous studies have estimated potential exoplanet yields achievable with current implementation concepts (e.g., Quanz et al. 2022b; Kammerer et al. 2022). Kammerer et al. (2022) determined that a LIFE setup targeting FGK-type stars and comprising 3.5 m mirrors and a total throughput of 5% is expected to detect 20_{-11}^{+20} EECs, assuming optimistic exoplanet occurrence rates. By extending the boundaries of potentially habitable planets to the optimistic HZ definition according to Kopparapu et al. (2014), the yield increases to 51_{-27}^{+50} planets. Comparable yields could be achieved with ≥ 2 m mirrors and a throughput of 20%. Although challenging, the N_P requirements we have identified for CO₂ trend detection and differentiation fall within the 1σ uncertainties of yield predictions in the respective scenarios. While a science case as this could inform critical instrumentation design, it similarly drives the advancement of robust atmospheric characterization frameworks.

4.2. Characterization Biases

We saw above that biases in parameter estimates provided by our atmospheric retrieval pipeline contribute to biased population-level trend inferences. While these play a minor role in trend detection, observational biases impact the ability to correctly differentiate biotic

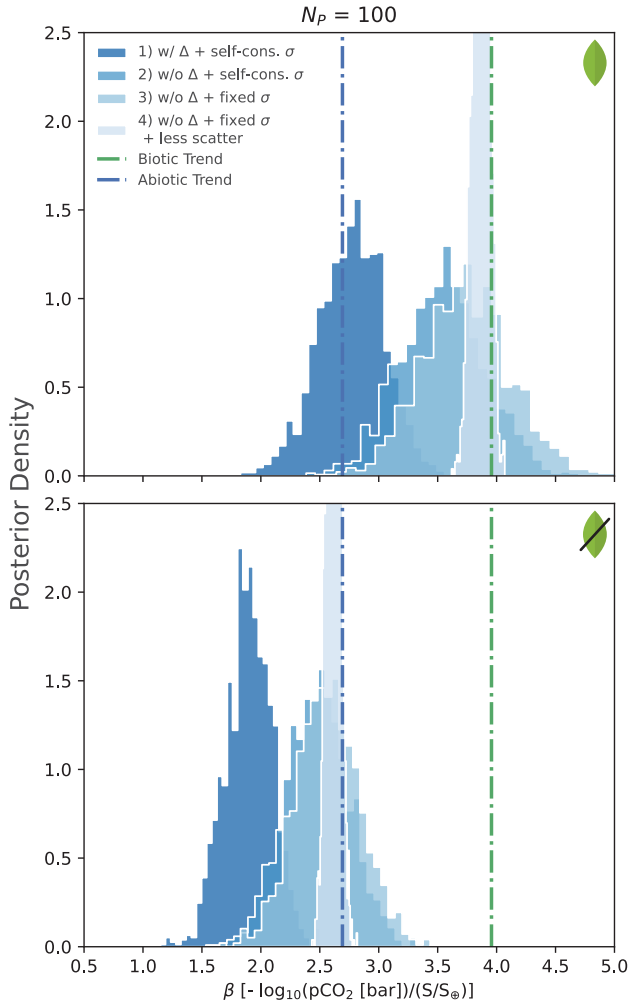


Figure 10. Comparison of trend distinction performance across four model assumptions in biotic (top) and abiotic (bottom) scenarios: 1) Base scenario, 2) No offset scenario, 3) Fixed standard deviation scenario, and 4) Reduced scatter scenario. We limit the model comparison to population size $N_P = 100$ and spectrum quality $S/N = 20$ and $R = 100$.

from abiotic CO_2 trends. We discuss potential reasons for these pCO_2 constraint biases in Sections 4.2.1 and 4.2.2. In Section 4.2.3 we discuss the implications of these observational biases for a trend detection strategy.

4.2.1. Treatment of H_2O profiles in atmospheric retrievals

A contributing factor to systematic characterization biases, in form of offsets between retrieved posteriors and true pCO_2 , can be found in an incorrect parametrization of the H_2O abundance profile in the retrieval forward model. Here, we address the role of H_2O in constraining accurate CO_2 abundances with atmospheric retrievals and how abundance constraints can be improved. To clarify, we first address the biases in abundance estimates, specifically focusing on the vol-

ume mixing ratio (VMR). Later, we examine how these biases affect the retrieved partial pressures.

H_2O has multiple strong absorption bands in the mid-infrared wavelength range and varies over orders of magnitude in its abundance with altitude (see Figure 4). In our atmospheric population, we can additionally see a large variation in H_2O abundance profiles across our set of HZ characteristic atmospheres. It is, however, a common simplification of 1D atmospheric retrievals to assume vertically constant abundance profiles. While CO_2 does not vary significantly with altitude, the assumption of pressure-independent abundance profiles is an especially strong simplification in the case of H_2O .

To understand the impact of H_2O profile parametrization in the retrieval forward model on CO_2 abundance constraints, we compare retrieval results from two scenarios. The first scenario involves input emission spectra with variable H_2O profiles, which corresponds to our original analysis. The second scenario assumes vertically constant H_2O abundances in the input atmospheres. We derive vertically constant abundances by calculating the pressure-weighted average of the variable H_2O abundance profiles. Figure 11 illustrates the CO_2 and H_2O abundance posteriors, along with the retrieved $P - T$ profiles for the $\text{pCO}_2 = 10^{-4}$ bar and $S/S_\oplus = 1.0$ case. Here, we focus on the highest spectrum quality scenario.

When accounting for a variable H_2O profile in the input spectrum, we observe an offset in the CO_2 posteriors toward larger than ground truth abundances, with CO_2 overestimated by ~ 1 dex (Figure 11, top row). The retrieval struggles to accurately constrain H_2O abundance due to the strongly variable H_2O profile, yielding posteriors centered between surface and stratospheric abundances (see Appendix B for all scenarios). The retrieval selects an H_2O abundance and $P - T$ profile that best fit the strong H_2O features in the mid-infrared, leading to biased pressure estimates due to the incorrect treatment of the H_2O profile in the forward model. This results in an underestimated surface pressure and a shift of the retrieved $P - T$ profile toward lower than ground truth pressures (see Appendix B for all scenarios). Similar biases have been observed in previous studies using the same retrieval pipeline with pressure-dependent H_2O profiles in the input spectra (Alej et al. 2022; Mettler et al. 2024). The underestimation of pressure correlates with an overestimation of retrieved CO_2 abundances due to a degeneracy between atmospheric species abundances and pressure broadening of spectral lines (Misra et al. 2014; Schwieterman et al. 2015; Alej et al. 2022; Mettler et al. 2024). This degeneracy between abundances and atmospheric pressure explains the overestimated CO_2 content.

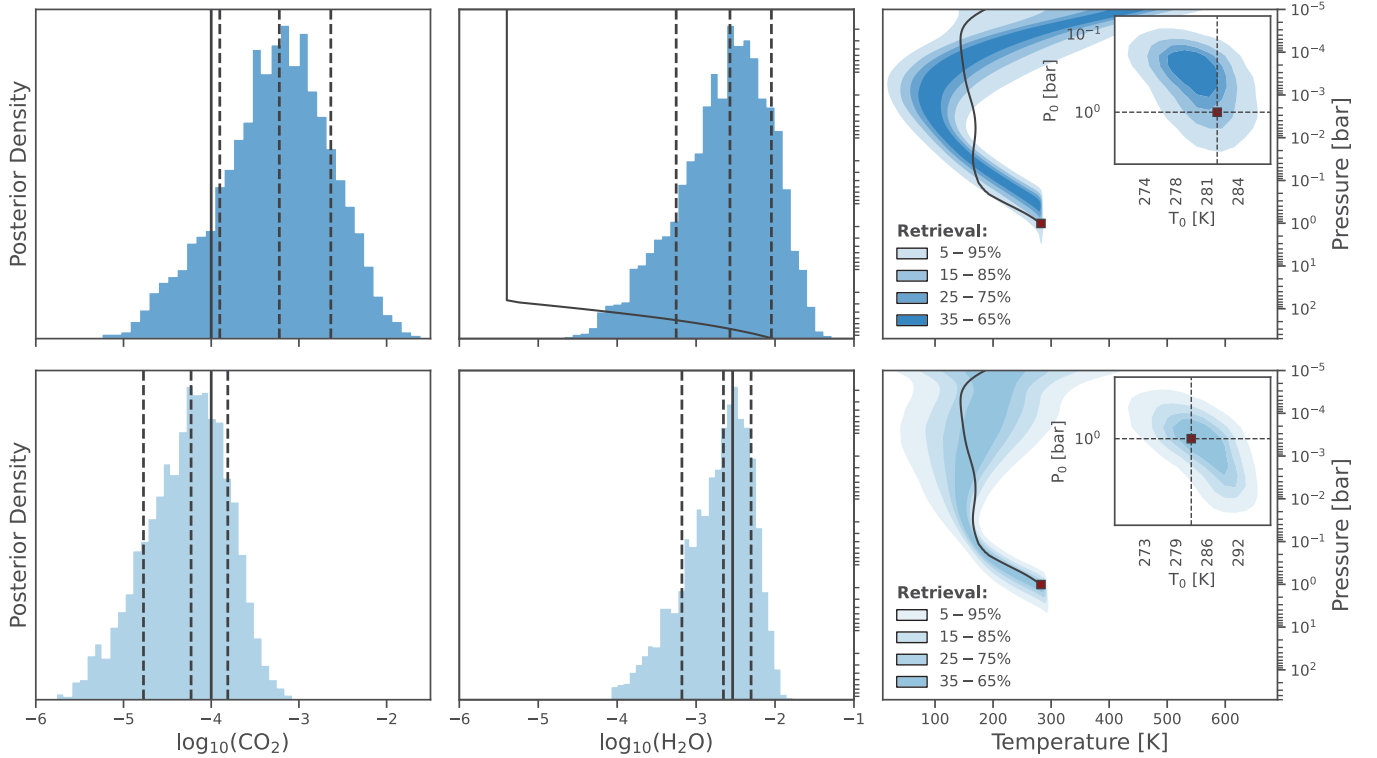


Figure 11. Comparison of atmospheric retrieval results between variable (top) and constant (bottom) H₂O profiles in the input spectrum of the $p\text{CO}_2 = 10^{-4}$ bar and $S/S_{\oplus} = 1.0$ scenario, for an observational sensitivity of $S/N = 20$ and $R = 100$. We show, from left to right, retrieved CO₂ abundance, H₂O abundance and $P - T$ profile constraints. Solid black lines indicate the ground truths, while dashed black lines denote the posterior median and 1σ envelope. The inset in the $P - T$ profile panel illustrates the retrieved constraints on surface conditions.

We then analyze results from input atmospheres with vertically constant H₂O abundances (Figure 11, bottom row). In these cases, H₂O abundances are accurately and precisely constrained, as our H₂O profile model matches the input profile. This improved H₂O estimation leads to retrieved thermal structures better centered around ground truths, which in turn results in CO₂ abundance posteriors more accurately centered around true values. Retrieval results for the vertically constant H₂O input profiles are presented for the complete atmospheric population in Appendix B.

Further evidence supporting the impact of H₂O parametrization on pressure and CO₂ constraint biases is provided by Konrad et al. (2024). The authors implemented a physical water condensation representation in the retrieval framework, resulting in improved characterization performance through a more accurate retrieval of atmospheric species abundances and thermal profiles for an Earth-twin case. However, preliminary attempts to constrain H₂O profiles with this refined parametrization for one of the atmospheric cases considered here showed limited characterization improvements. Future work could further test the flexibility of the physical water condensation framework on the generated atmo-

spheric population and assess implications for detecting population-level CO₂ trends.

4.2.2. Characterization Potential of Atmospheres at the Habitable Limit

Constraining surface conditions in the $p\text{CO}_2 \geq 1$ bar parameter space introduces an additional characterization bias. We examine the characterization potential of CO₂-dominated atmospheres at the habitable limit of our atmospheric population, focusing on retrieved constraints for CO₂ partial pressures, surface pressures P_0 , and H₂O abundances, as visualized in Figure 12. Three habitable edge cases are analyzed - two at the high-temperature and one at the low-temperature limit.

Case 1 ($T_0 > 330$ K): We derive SL posteriors for $p\text{CO}_2$ and surface pressure P_0 . While lower bounds for these parameters are retrieved, upper limits remain unconstrained. As outlined in Section 3.2, $p\text{CO}_2$ constraints are calculated by multiplying P_0 with CO₂ abundance posteriors. Consequently, sensitivity limits on the surface pressure P_0 similarly influence SL-constraints on CO₂ partial pressures. H₂O abundances are constrained to stratospheric levels, suggesting that only the upper atmosphere is being probed. This indi-

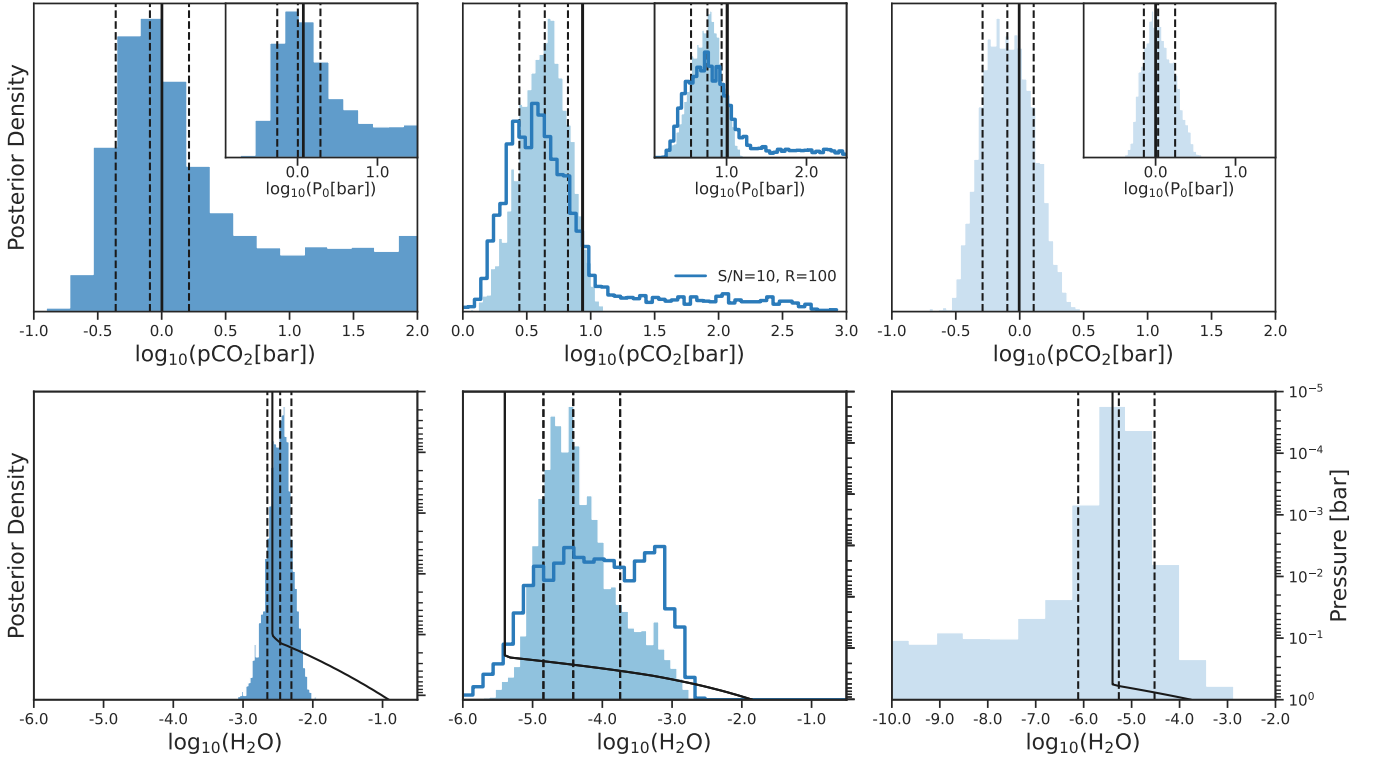


Figure 12. Atmospheric retrieval results for three CO_2 -dominated scenarios from our atmospheric population. Case 1 (left): $p\text{CO}_2 = 1$ bar, $S/S_\oplus = 1.0$; Case 2 (center): $p\text{CO}_2 = 10$ bar, $S/S_\oplus = 0.4$; and Case 3 (right): $p\text{CO}_2 = 10$ bar, $S/S_\oplus = 0.4$. The top row illustrates the posterior distributions for the retrieved $p\text{CO}_2$ and P_0 parameters, while the bottom row shows estimated H_2O abundances for each case. All retrievals were performed using simulated observations with $S/N = 20$ and $R = 100$. Solid black lines indicate the ground truths, while dashed black lines denote the posterior median and 1σ envelope. In SL posterior cases, we show median and 1σ envelope of the sensitivity peak.

icates that the high H_2O content ($\sim 10\%$) and temperature (see Figure 4) result in an optically thick lower atmosphere, restricting our ability to determine surface conditions. This limitation is consistent with the retrieved P_0 constraints.

Case 2 ($T_0 > 330$ K): In this scenario, both CO_2 partial pressures and surface pressure P_0 are underestimated, with the ground truth falling outside the 1σ posterior envelope. This contrasts with observations in the $p\text{CO}_2 < 1$ bar parameter space, where underestimated P_0 constraints are associated with overestimated CO_2 partial pressures. The $p\text{CO}_2$ constraints correspond to the product of P_0 and CO_2 VMR posteriors. In the $p\text{CO}_2 \geq 1$ bar parameter space, CO_2 VMRs are tightly constrained at the upper prior edge, causing $p\text{CO}_2$ posteriors to closely follow surface pressure constraints, explaining the tendency for negative offsets. The retrieved H_2O abundance constraint indicates atmospheric probing below stratospheric levels, corresponding to the non-constant regime of the H_2O abundance profile. This is typical for most atmospheric scenarios in our population. The incorrect treatment of the H_2O profile as vertically constant in the retrieval forward model leads

to biased surface pressure constraints. Additionally, a spectrum quality dependence is observed for CO_2 partial pressure and surface pressure constraints. At $S/N = 10$, only SL constraints are obtained for both parameters, indicating reduced capabilities to infer surface conditions.

Case 3 ($T_0 < 250$ K): In this low temperature case, we are able to accurately constrain $p\text{CO}_2$ (ground truth within 1σ posterior envelope). Residing at the outer edge of the HZ with a CO_2 partial pressure of 1 bar, this atmosphere contains the lowest H_2O abundance within the atmospheric sample considered here. Driven by the low atmospheric H_2O content and low overall emitted flux of this cold outer HZ planet (see Figure 4), we can only derive an upper limit for the H_2O abundance. In the context of constraining accurate CO_2 partial pressures, low H_2O mixing ratios do not have further implications.

In summary, negative $p\text{CO}_2$ constraint offsets in the $p\text{CO}_2 \geq 1$ bar parameter space are similarly driven by the assumption of constant H_2O profiles within the retrieval. However, these offsets exhibit an opposite bias in $p\text{CO}_2$ constraints compared to $p\text{CO}_2 < 1$ bar cases,

attributable to the high CO₂ content. CO₂ abundances are tightly constrained at the upper prior limit, precluding overestimation. Hence, the retrieved pCO₂ in this parameter space closely follows the P_0 constraint, which is typically underestimated due to the retrieval’s difficulty in accurately determining H₂O abundances, as observed in most scenarios within our population. Furthermore, optically thick lower atmospheres naturally limit the ability to constrain surface conditions using mid-infrared thermal emission spectra. However, in the context of this study, the impact on pCO₂ constraint capabilities remains limited, as we exclusively consider SL-limited posteriors for their Gaussian sensitivity peaks (see Section 3.2). The CO₂ partial pressures we retrieve here are sufficiently constrained to introduce only minor biases to our CO₂ trend detectability assessment.

4.2.3. Implications for Trend Detection Capabilities

We identify characterization biases based on simplified species profile parametrization in retrieval forward models. Though the respective implications for CO₂ partial pressure constraints vary depending on the atmosphere’s location in the 2D pCO₂- S parameter space, these biases are visible across the atmospheric population investigated here. As a consequence, these biases translate to biased CO₂ trend detections. We predict that atmospheric characterization biases might readily be reduced by applying a more accurate, physical parametrization of e.g. H₂O, as an important opacity source in the mid-infrared spectral range that shows orders of magnitude variability within HZ characteristic atmospheres. This, necessarily, demands for forward models and retrieval routines in general, that are robust against population-scale atmospheric diversity.

In addition, the information content retrievable from thermal emission spectra is naturally limited by optically thick atmospheric layers. Especially at the high temperature edge of the HZ, we are likely to encounter large H₂O abundances driving optically thick lower atmospheres, masking deeper contributions to the spectrum. Although accurate constraints of high CO₂ abundances might still be possible here, the inference of surface conditions is rather challenging in these cases. A potential lack of well-constrained surface conditions at the high temperature habitability edge may reduce the parameter space of survey populations accessible to trend detection assessments.

4.3. Limitations

In this study we show that population-level CO₂ trends can readily be detected with LIFE observations of a population of terrestrial HZ atmospheres. In contrast,

differentiating biotic from abiotic CO₂ trends poses challenges that require advancements in our present atmospheric characterization frameworks. While LIFE serves as a specific case study, these findings are widely relevant to any future space-based mid-infrared mission designed to perform these population-scale atmospheric characterizations. To set these results into broader context, we outline the limitations of this work.

First, our atmospheric model assumes a simplified composition consisting of CO₂, H₂O and N₂. However, we can expect actual atmospheric populations to show greater diversity in compositions than considered here (for a review, see, e.g., [Wordsworth & Kreidberg 2022](#)). The inclusion of additional species, such as CH₄ or O₃, would influence the self-consistent modeling of planetary atmospheres, impacting thermal structures and surface conditions. Moreover, the presence of other atmospheric components may affect the ability of the retrieval to constrain CO₂ abundances in multiple ways. For instance, overlapping absorption bands, such as those of O₃ and CO₂ (both at $\sim 10 \mu\text{m}$) or CH₄ (around $8 \mu\text{m}$) and H₂O (ranging from 5 to $8 \mu\text{m}$) (e.g., [Konrad et al. 2022](#)), along with the increased complexity introduced by additional parameters in the retrieval, could impact the precision of CO₂ abundance estimates.

The influence of clouds is neglected in both the input spectra and the retrieval forward model. This assumption is particularly relevant in the high surface temperature regime, where clouds would impact atmospheric characterization due to the expected high atmospheric water content. However, clouds have a significantly smaller effect on mid-infrared radiation than on reflected stellar light (e.g. [Kitzmann et al. 2011](#); [Marley et al. 2013](#); [Fauchez et al. 2019](#)). Nevertheless, previous studies have examined the performance of the retrieval framework employed in this study in the context of cloudy Earth-like emission spectra. On Earth, patchy H₂O cloud coverage partially obstructs thermal emissions from lower atmospheric layers. Both [Alej et al. \(2022\)](#) and [Mettler et al. \(2024\)](#) conducted atmospheric retrievals on cloudy emission spectra while assuming a cloud-free atmosphere, leading to biases in their inferred atmospheric and planetary parameters. Specifically, [Mettler et al. \(2024\)](#) identified biases in the retrieved surface temperature and planetary radius estimates, which were attributed to the omission of cloud effects. These findings were further validated by [Konrad et al. \(2024\)](#), who demonstrated that incorporating clouds into the retrieval forward model mitigates biases in the retrieved temperature and radius estimates. In addition to H₂O cloud formation, the condensation of CO₂ and the subsequent development of CO₂ clouds

become significant at the outer edge of the HZ, leading to a complex interplay between radiative warming and cooling effects on planetary climates (e.g., [Forget & Pierrehumbert 1997](#); [Kitzmann 2017](#)). On this basis, future studies should explore the implications of both H₂O and CO₂ clouds for the performance of atmospheric retrievals applied across a broad population of HZ characteristic atmospheres and investigate their impact on the detectability of population-level CO₂ trends.

Moreover, we neglect photochemical processes in our HZ characteristic atmospheric population. In Earth’s atmosphere we observe a considerable altitude-dependence of certain species, e.g. H₂O and O₃, which are driven by photochemical reactions in the stratosphere (e.g. [Chapman 1932](#); [Jones et al. 1986](#)). Consequently, assuming constant abundance profiles may introduce biases in the retrieved abundance estimates. In contrast, CO₂ is well mixed throughout the atmosphere, making the assumption of a constant abundance profile a sufficient approximation (e.g., [Rugheimer & Kaltenecker 2018](#); [Mettler et al. 2024](#)). Omitting photochemistry may further impact the self-consistent modeling of planetary atmospheres. For instance, in the case of Earth, photochemical O₃ induces a temperature inversion in the $P - T$ profile, which subsequently influences Earth’s mid-infrared emission spectrum.

In our retrieval pipeline we parametrize atmospheric thermal structures with a fourth order polynomial. This model allow us to be flexible in the types of $P - T$ profiles that we fit within the retrieval. However, the higher the number of parameters is, the more computationally expensive the retrieval becomes. In context of providing an accurate thermal structure fit with a relatively low number of parameters, a learning-based $P - T$ profile parametrization could provide a powerful alternative ([Gebhard et al. 2024](#)). Additionally, the learning-based approach would guarantee physical thermal profiles, whereas a polynomial parametrization cannot inherently exclude unphysical ones. Currently, there is, however, a lack of $P - T$ profile training data in the temperate terrestrial atmosphere regime which limits the reliability of this approach. Especially in context of atmospheric characterization on a population-level, these models need to be equipped with a broad swath of thermal structures to depict a wide atmospheric variety.

Our grid of 12 atmospheric states is a discrete representation of characteristic HZ atmospheres and cannot represent the full atmospheric diversity that can be expected in real terrestrial HZ atmospheres. We assume all planets to be located at 10 pc from the observer orbiting a G2V star and consisting of Earth-like planetary parameters, such as planetary radius and surface grav-

ity. This approach is justified, since the grid has the primary function to interpolate retrieval results without the need to perform large-scale, computationally intensive, retrievals on the order of population sizes ($N_P \leq 100$) that we investigate here. Naturally, the estimated pCO₂ posterior maps cannot be translated to arbitrary atmospheric cases but need to be understood within the context of our atmospheric population and respective assumptions. Furthermore, the accuracy of interpolating between posteriors of various atmospheric scenarios as a proxy for direct retrieval results remains uncertain, warranting further investigation to understand the potential and limitations of this approach.

The aim of the present study is to test observational capabilities to detect and constrain population-level CO₂ trends. However, [Lehmer et al. \(2020\)](#) suggested differentiating between the 2D pCO₂- S population and a uniform population within habitable temperature limits to achieve an unambiguous test for a functioning Cb-Si cycle. A linear null trend, following the null (uniform) population defined after [Lehmer et al. \(2020\)](#), would be naturally more challenging to reject than a flat trend. However, this null trend definition relies on assumptions of shape and extent of a null population. Given the lack of a well-characterized Cb-Si null population, we consider the absence of correlation (i.e., a flat trend) in CO₂ partial pressures with stellar irradiation to be the more robust null hypothesis in our trend assessment context.

Besides detecting population-level CO₂ trends, we assess the potential to differentiate biotic from abiotic CO₂ trends. Given that we have only one instance of a Cb-Si world that, coincidentally or not, evolved to host a biosphere, we lack predictions for a corresponding abiotic scenario. Therefore, as previously outlined, we restrict the biotic enhancement of chemical weathering in the Cb-Si model ([Krissansen-Totton & Catling 2017](#); [Krissansen-Totton et al. 2018](#); [Lehmer et al. 2020](#)) to generate a second pCO₂- S population with minimal biotic influence on the Cb-Si weathering feedback mechanism. Consequently, our biotic Cb-Si distribution encompasses a broad variability of biotic impact on the weathering feedback, with the abiotic distribution corresponding to a subset of this. However, these distributions likely do not provide an accurate representation of reality. We might observe a stronger mix of Cb-Si populations with decisive and weak biotic impact, a mix of worlds with and without functioning Cb-Si cycles or potentially no indicators of a trend in CO₂ abundance with stellar irradiation whatsoever. Future work could investigate biases in trend detection by exploring more complex mixed populations, which would still require as-

sumptions about the respective biotic, abiotic, and null Cb-Si distributions. Importantly, the Cb-Si populations considered here serve as cases to test observational capabilities against. Thereby, we initiate a pathway toward gaining insight into the actual presence and characteristics of Cb-Si driven CO₂ trends by equipping future missions with the necessary capabilities to ultimately test these hypotheses empirically.

5. SUMMARY AND CONCLUSIONS

In this study, we investigated how a trend in CO₂ abundance with stellar irradiation can be detected from thermal emission spectra of a population of temperate terrestrial exoplanet atmospheres. We explored this trend as tracer for the Cb-Si weathering cycle, a population-level habitability signature. Additionally, we assessed the ability to differentiate between CO₂ trends in atmospheric populations with global-scale biospheres and largely abiotic worlds, examining the observational feasibility of CO₂ trends as population-level indicators of global biotic activity. We created synthetic exoplanet survey populations with atmospheric compositions based on geochemistry-climate predictions and performed retrievals on simulated LIFE observations of the planets' thermal emission. Using a hierarchical importance sampling formalism, we inferred trend constraints, assessing the diagnostic power of a population-scale characterization approach.

We observe a robust detection of CO₂ trends for population sizes $N_P \geq 30$ and all considered spectrum quality scenarios $S/N = [10, 20]$ and $R = [50, 100]$ in both biotic and abiotic cases. The strength of trend detection is predominantly influenced by N_P , while largely independent of the considered S/N and R assumptions. We obtain overall higher confidence in trend detection in the biotic than the abiotic case. This observation is associated with the difference in pCO₂- S parameter space covered by predicted biotic and abiotic Cb-Si distributions. Notably, we observe a tendency to underestimate CO₂ trend slopes, which does not play a major limiting factor in trend detection but influences the assessed capabilities to correctly differentiate biotic from abiotic CO₂ trends.

In context of differentiating between biotic and abiotic trends, we find that both accuracy (centering of trend slope estimate around true trend) and precision (tightness of trend estimate) play significant roles. We find the retrieved trend slope constraints to be consistently offset from the ground truths, which leads to a biased characterization of biotic and abiotic CO₂ trends. By investigating drivers of these trend offsets, we find biases in individual planet pCO₂ constraints to be a major fac-

tor for trend constraint accuracy, whereas the number of characterized atmospheres N_P as well as the underlying variability of true pCO₂ within the population represent significant factors for trend constraint precision. If pCO₂ constraint biases were corrected, biotic and abiotic population trends could be accurately constrained for $N_P \geq 100$.

We identify two classes of pCO₂ constraint biases. The first bias is driven by the widely applied simplification of vertically constant atmospheric species profiles in the retrieval forward models. Here, H₂O plays a significant role due to its large variability in HZ characteristic atmospheres and its strong mid-infrared opacity which greatly influences the retrieval performance and respective constraints on CO₂ abundances. However, further advancements are needed to develop retrieval frameworks that remain robust against population-scale atmospheric diversity. The second pCO₂ constraint bias is driven by limited capabilities to retrieve surface pressure constraints on high surface temperature habitability edge cases. Here, large water vapor abundances lead to optically thick lower atmospheres, which naturally prohibit the probing of surface layers via thermal emission spectra. While this bias has only limited impact on our trend assessment here, it represents an inherent characterization limitation for atmospheres at the upper-temperature bound of the HZ.

We demonstrate the ability of future missions like LIFE, or similar mid-infrared interferometer concepts, to enable population-level characterization of temperate terrestrial atmospheres and find that Cb-Si cycle driven CO₂ trends, as population-wide habitability signature, can readily be detected in a modest population of thermal emission spectra. However, we are only beginning to explore the potential of comparative planetology in terrestrial exoplanet atmospheres. Further studies, which test atmospheric characterization performance against broad atmospheric diversity, are essential to prepare next-generation observational facilities to provide robust and accurate constraints of atmospheric as well as planetary parameters. Then, efforts like these will pave the way toward assessing the commonness of habitable worlds or even global-scale biospheres outside of our Solar System.

J.H., S.P.Q., and D.V. thank the ETH Centre for Origin and Prevalence of Life for its generous financial support. Parts of this work have been carried out within the framework of the National Centre of Competence in Research PlanetS supported by the Swiss National Science Foundation under grants 51NF40_205606, 51NF40_182901, and 200020_200399. J.H., S.P.Q., D.A., B.S.K., E.G., and F.A.D. acknowledge the financial support of the SNSF. E.A.’s research was supported by an appointment to the NASA Postdoctoral Program at the NASA Goddard Space Flight Center, administered by Oak Ridge Associated Universities under contract with NASA. The authors would also like to thank Owen Lehmer, Joshua Krissansen-Totton, Jacob Lustig-Yaeger and Sandra Bastelberger for their expertise and useful discussions.

Author Contributions: J.H. carried out the analyses, created the figures, developed the software, and wrote the original manuscript. S.P.Q., D.A., and D.V. initiated the project and provided regular guidance, supervision, and conceptual input. B.S.K. and E.G. provided expertise on atmospheric retrieval and statistical analysis, respectively. J.K. contributed synthetic planet population data generated with P-Pop. All authors reviewed and edited the manuscript.

Data Availability: All source data underlying the results of this study, including spectral data and retrieved parameter posterior distributions, have been archived on Zenodo (Hansen et al. 2025). The dataset is accessible at <https://zenodo.org/records/15056424>.

Software: This work has made use of several open source packages, including `matplotlib` (Hunter 2007), `numpy` (Harris et al. 2020), `pandas` (Wes McKinney 2010), `petitRADTRANS` (Mollière et al. 2019, 2020; Alei et al. 2022), and `scipy` (Virtanen et al. 2020).

APPENDIX

A. TREND STATISTICS: PRELIMINARY HYPOTHESIS TESTING

To obtain a first understanding of the observational feasibility associated with detecting and differentiating biotic and abiotic CO₂ trends in a population of temperate terrestrial atmospheres, we perform a set of preliminary frequentist hypothesis tests which assume a fixed population-wide observational constraint on CO₂ partial pressures. This approach allows for a systematic evaluation of the relationship between observational uncertainty, sample size, and the ability to detect atmospheric CO₂ trends across diverse planetary populations.

A.1. Hypothesis Test Setup

We infer the required number of planets to detect atmospheric CO₂ trends based on the assumed observational uncertainty of atmospheric CO₂ partial pressure. Synthetic survey populations with up to $N_P = 100$ planets per sample are constructed. For each N_P scenario, incident flux values S are drawn for each planet from a characteristic EEC distribution estimated from simulated LIFE observations (Section 2.1, Figure 2). Each planet is then assigned a true atmospheric pCO₂ value, dependent on its received stellar irradiation. The pCO₂ level is drawn from either biotic or abiotic 2D pCO₂- S distributions (Section 2.2, Figure 3), depending on the scenario being tested. Each (pCO₂, S) pair is associated with a simplified observational uncertainty $\delta\text{pCO}_2 = \pm[0.1, 0.5, 1.0, 1.5]$ dex around the true pCO₂, with the uncertainty level fixed across a given survey population. For each population size and observational uncertainty scenario, (pCO₂, S) pairs are redrawn 10,000 times using bootstrapping with sample replacement. A weighted least squares (WLS) fit is performed for each instance to enable marginalization over the trend population for given sample size and uncertainty. In order to infer capabilities to detect and differentiate biotic and abiotic CO₂ trends, we conduct t-tests on the slope parameter, based on the following three hypothesis:

- $\mathcal{H}_0: \beta = 0, \mathcal{H}_1: \beta \neq 0$: We test the detectability of a semi-logarithmic CO₂ trend by testing the rejection of a null (flat) trend, where β represents the logarithmic slope. This test is performed for both biotic and abiotic scenarios.
- $\mathcal{H}_{0,bio}: \beta = \beta_{abio}, \mathcal{H}_{1,bio}: \beta \neq \beta_{abio}$: We assess the differentiation between biotic and abiotic CO₂ trends by testing whether an abiotic trend can be rejected in the biotic scenario.
- $\mathcal{H}_{0,abio}: \beta = \beta_{bio}, \mathcal{H}_{1,abio}: \beta \neq \beta_{bio}$: We assess the differentiation between biotic and abiotic CO₂ trends by testing whether a biotic trend can be rejected in the abiotic scenario.

A hypothesis is considered rejected if the estimated p-value < 0.05 . We conduct two-tailed tests to allow for detection sensitivity of either effect direction. These tests are conducted on 10,000 fitted trends per survey population size and observational uncertainty case, yielding a set of 10,000 test outcomes for each N_P and δpCO_2 scenario. We estimate the minimum number of planets required to achieve a given fraction (statistical power) of the 10,000 tests that correctly reject the respective false null hypotheses (p-value < 0.05). This approach allows us to examine the necessary population size and observational uncertainty levels required to achieve 95%, 99%, and 99.9% likelihood of identifying trends, assuming these trends are present within the atmospheric population (see [Checlair \(2021\)](#) for a comparable trend statistical analysis framework).

The left panel in Figure 13 illustrates the inference of minimum population sizes based on our hypothesis testing. This panel displays test outcomes for rejecting a flat trend (first hypothesis test) in the biotic scenario. The intersection of curves representing equal statistical power and the statistical significance threshold indicates the required magnitude of N_P . For instance, to achieve a 95% rate of correctly rejecting the false null hypothesis of a flat trend, assuming $\delta\text{pCO}_2 = 1.0$ dex, a minimum of 23 EEC observations is necessary.

A.2. Hypothesis Test Results: Sensitivity of CO₂ Trend Detection and Differentiation

First we investigate the detectability of population-level CO₂ trends in both biotic and abiotic scenarios, focusing on the minimum required population sizes N_P to achieve a statistical power between 95% and 99.9% across various observational uncertainty scenarios. The analysis shown in the top row of Figure 13 illustrates results for pCO₂ drawn

from biotic (left) and abiotic (right) Cb-Si distributions. Key findings indicate that larger observational uncertainties in atmospheric CO_2 partial pressure necessitate higher numbers of planets to reject a null trend at a given statistical power. Additionally, fewer planets are required to reject the null trend in biotic distributions compared to abiotic distributions, attributed to the flatter shape of the abiotic distribution in the 2D $p\text{CO}_2$ - S parameter space (Figure 3). For an observational uncertainty of $\delta p\text{CO}_2 = 0.5$ dex, ≥ 34 planets are required to reject a flat population-level CO_2 trend at the highest considered statistical power in both biotic and abiotic cases.

We also assess the ability to differentiate between biotic and abiotic CO_2 trends (Figure 13, bottom row), revealing larger required population sizes to reject respective null hypotheses compared to rejecting a null trend. Fewer planets are needed to reject a biotic trend in the abiotic scenario than vice versa, due to the distribution and location of the respective 2D $p\text{CO}_2$ - S distributions. Since the abiotic distribution corresponds to a subpopulation of the biotic one, an abiotic trend is harder to reject when sampling from the (full) biotic parameter space. For observational uncertainties ≥ 0.5 dex, both null hypothesis rejections generally require > 100 observed EEC atmospheres.

In conclusion, detecting population-level CO_2 trends requires fewer observations or allows for larger observational uncertainties compared to differentiating between biotic and abiotic population trends. Our hypothesis tests highlight a strong sensitivity of trend detectability to both observational uncertainty and available planet population sizes, as well as differences in trend detection capabilities between biotic and abiotic cases, which are linked to the respective distributions in the 2D $p\text{CO}_2$ - S parameter space. These observed sensitivities underscore the importance of more nuanced estimates of observational uncertainty, as demonstrated in our main trend detection analysis, and emphasize the necessity of assessing broad survey population sizes to effectively address both trend detection and differentiation between biotic and abiotic trends.

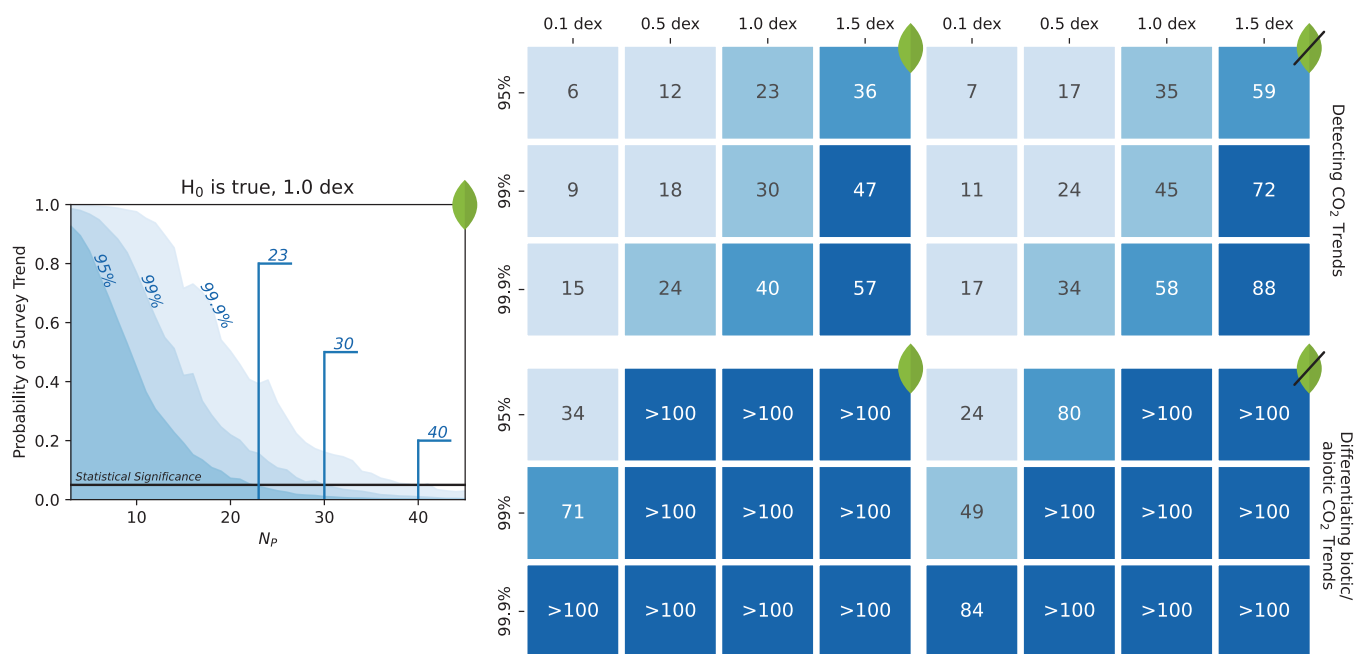


Figure 13. Minimum population sizes required to detect and differentiate biotic and abiotic CO_2 trends. Left: Visualization of the minimum population size inference approach. Right: Map of minimum required population sizes N_p to achieve statistical power between 95% and 99.9% across various observational uncertainty scenarios $\delta p\text{CO}_2$. Upper panels represent trend detection (first hypothesis test), while lower panels illustrate differentiation between biotic and abiotic trends (second and third hypothesis tests). Color gradients indicate the magnitude of N_p required under different $\delta p\text{CO}_2$ and statistical power scenarios.

B. SUPPLEMENTARY ATMOSPHERIC RETRIEVAL RESULTS

We show σ and Δ maps for all spectral quality cases in Figures 14 and 15, respectively. We visualize retrieved CO₂ partial pressures for all scenarios in our grid and all spectrum quality cases covering $S/N = [10, 20]$ and $R = [50, 100]$ in Figure 16. For all spectrum quality scenarios, we show retrieved posterior distributions for H₂O abundances in Figure 17 and retrieved $P - T$ profiles in Figures 18 - 21. Finally, in Figures 22 and 23, we present the CO₂ and H₂O abundances derived from atmospheric retrievals performed on simulated emission spectra, where H₂O profiles were assumed to be vertically constant in the input spectra.

- Figure 14 - Maps of posterior standard deviations (σ) for all spectrum quality cases.
- Figure 15 - Maps of posterior offsets (Δ) for all spectrum quality cases.
- Figure 16 - Retrieved CO₂ partial pressure posteriors.
- Figure 17 - Retrieved H₂O abundance posteriors.
- Figure 18 - Retrieved $P - T$ profiles for $S/N = 10$ and $R = 50$.
- Figure 19 - Retrieved $P - T$ profiles for $S/N = 10$ and $R = 100$.
- Figure 20 - Retrieved $P - T$ profiles for $S/N = 20$ and $R = 50$.
- Figure 21 - Retrieved $P - T$ profiles for $S/N = 20$ and $R = 100$.
- Figure 22 - Retrieved CO₂ abundance posteriors for constant H₂O profiles in input spectra.
- Figure 23 - Retrieved H₂O abundance posteriors for constant H₂O profiles in input spectra.

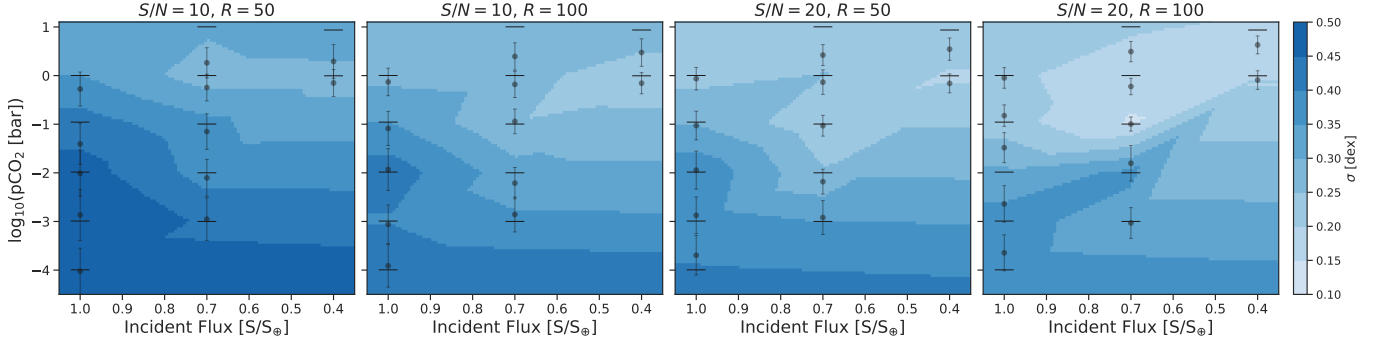


Figure 14. As top panel in Figure 6 but for spectrum quality cases $S/N = [10, 20]$ and $R = [50, 100]$.

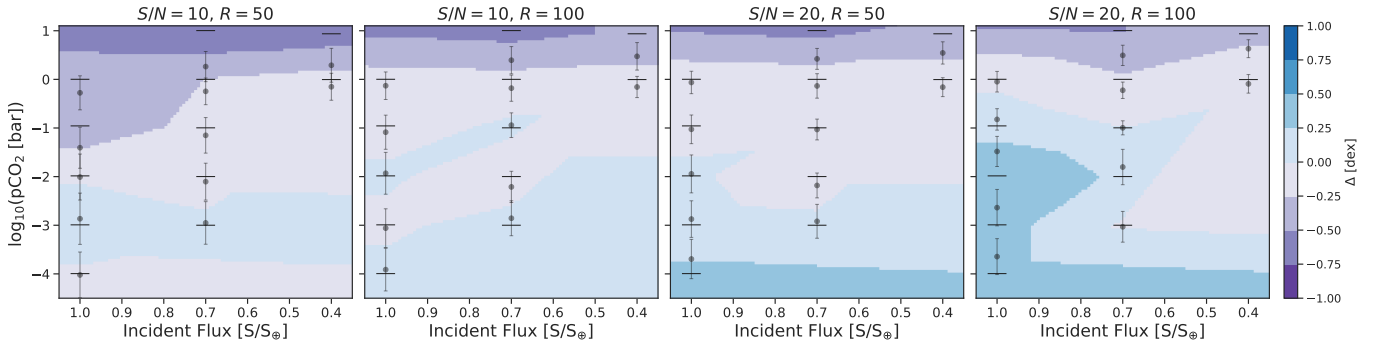


Figure 15. As bottom panel in Figure 6 but for spectrum quality cases $S/N = [10, 20]$ and $R = [50, 100]$.

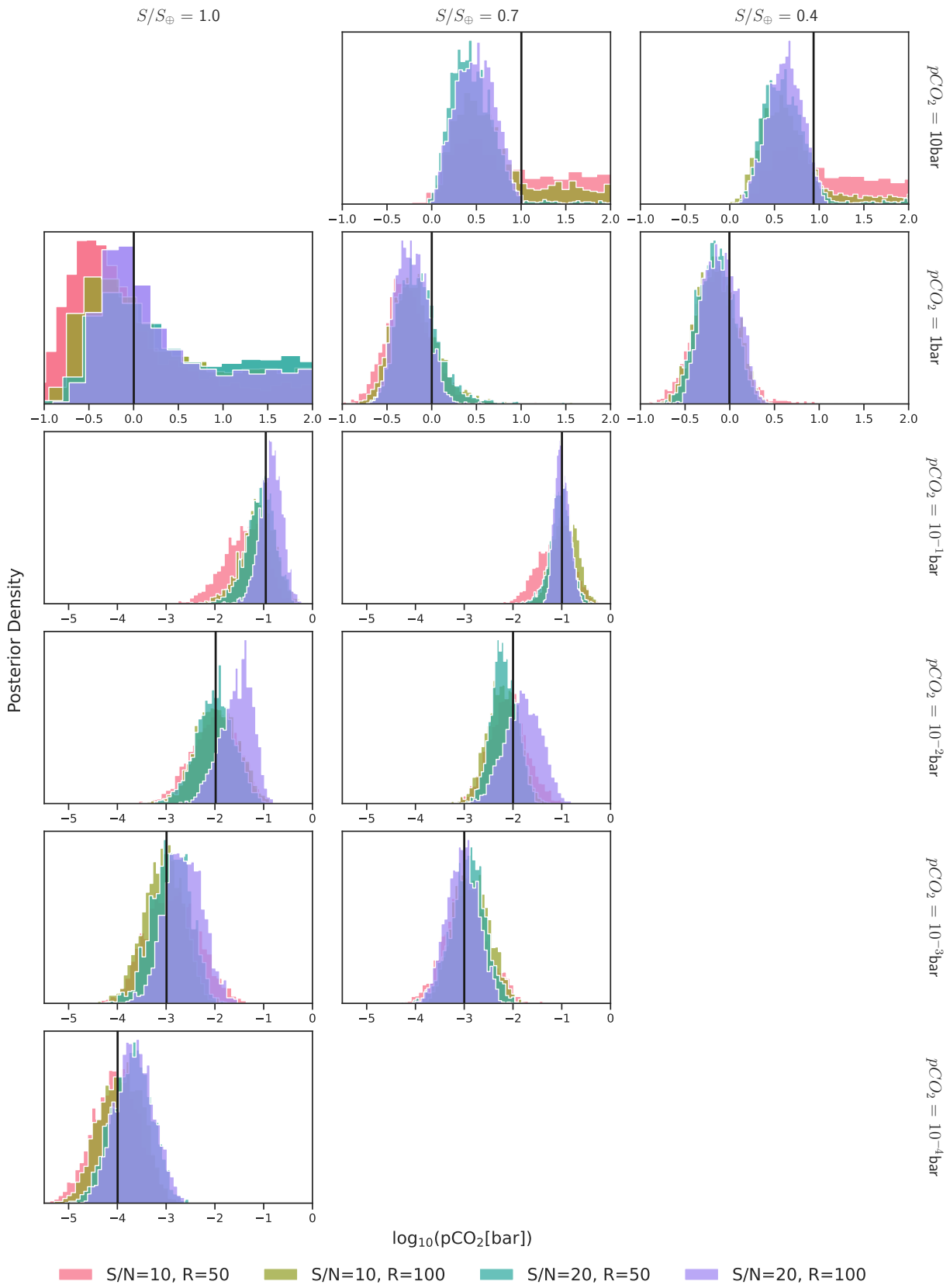


Figure 16. As Figure 5 but for CO₂ partial pressures.

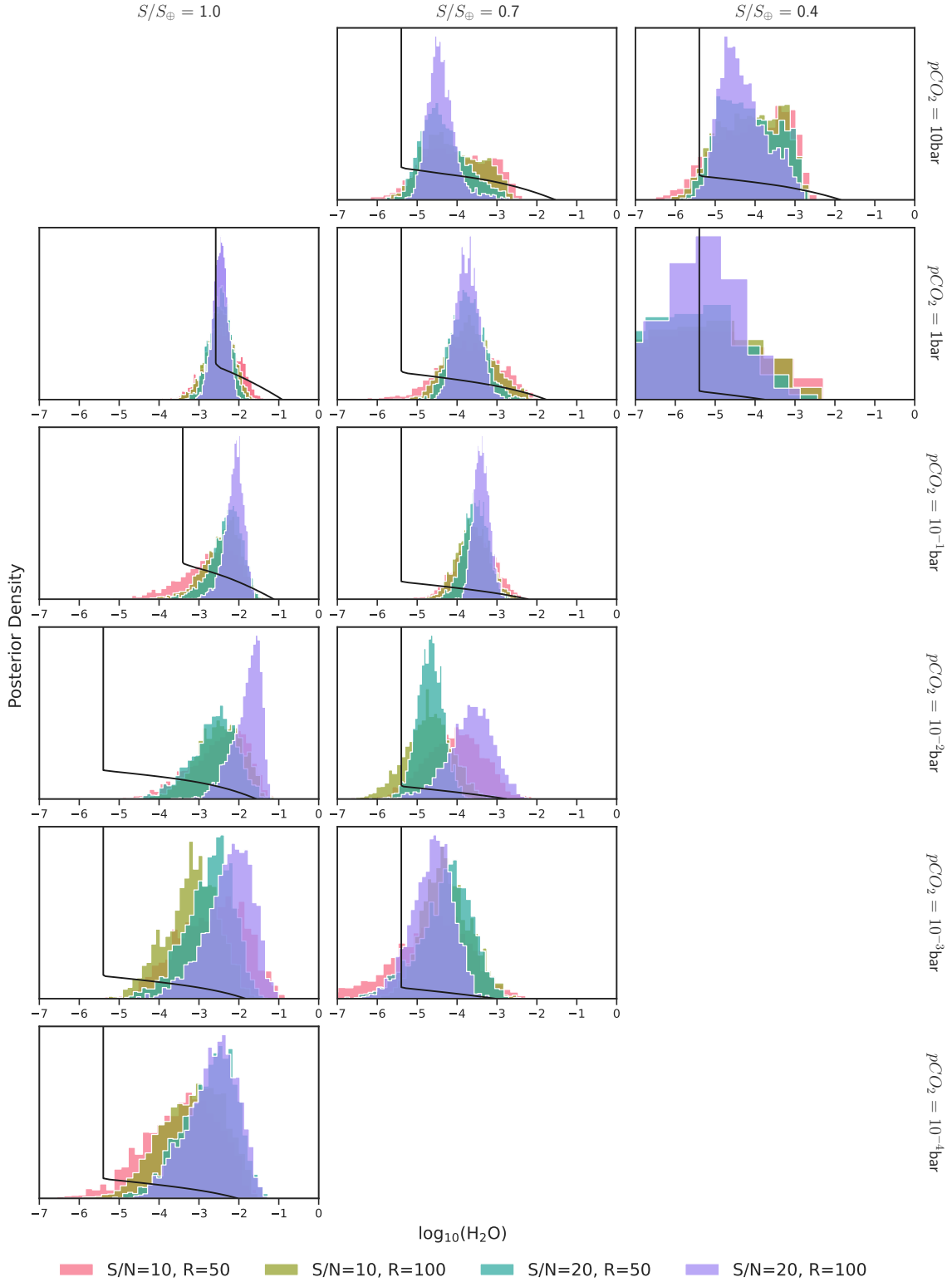


Figure 17. Posterior distributions of H₂O abundance derived from atmospheric spectrum retrievals. The panels are arranged to reflect the atmospheric grid within the pCO_2 - S parameter space. Columns represent different stellar insolation values, $S/S_{\oplus} = 1.0, 0.7, 0.4$, while rows correspond to different CO₂ partial pressures, $pCO_2 = 10 \text{ bar}, 1 \text{ bar}, 10^{-1} \text{ bar}, 10^{-2} \text{ bar}, 10^{-3} \text{ bar}, 10^{-4} \text{ bar}$. Each panel shows results for four combinations of signal-to-noise ratio, $S/N = [10, 20]$, and spectral resolution, $R = [50, 100]$. Thick black lines indicate the ground truth H₂O abundance.

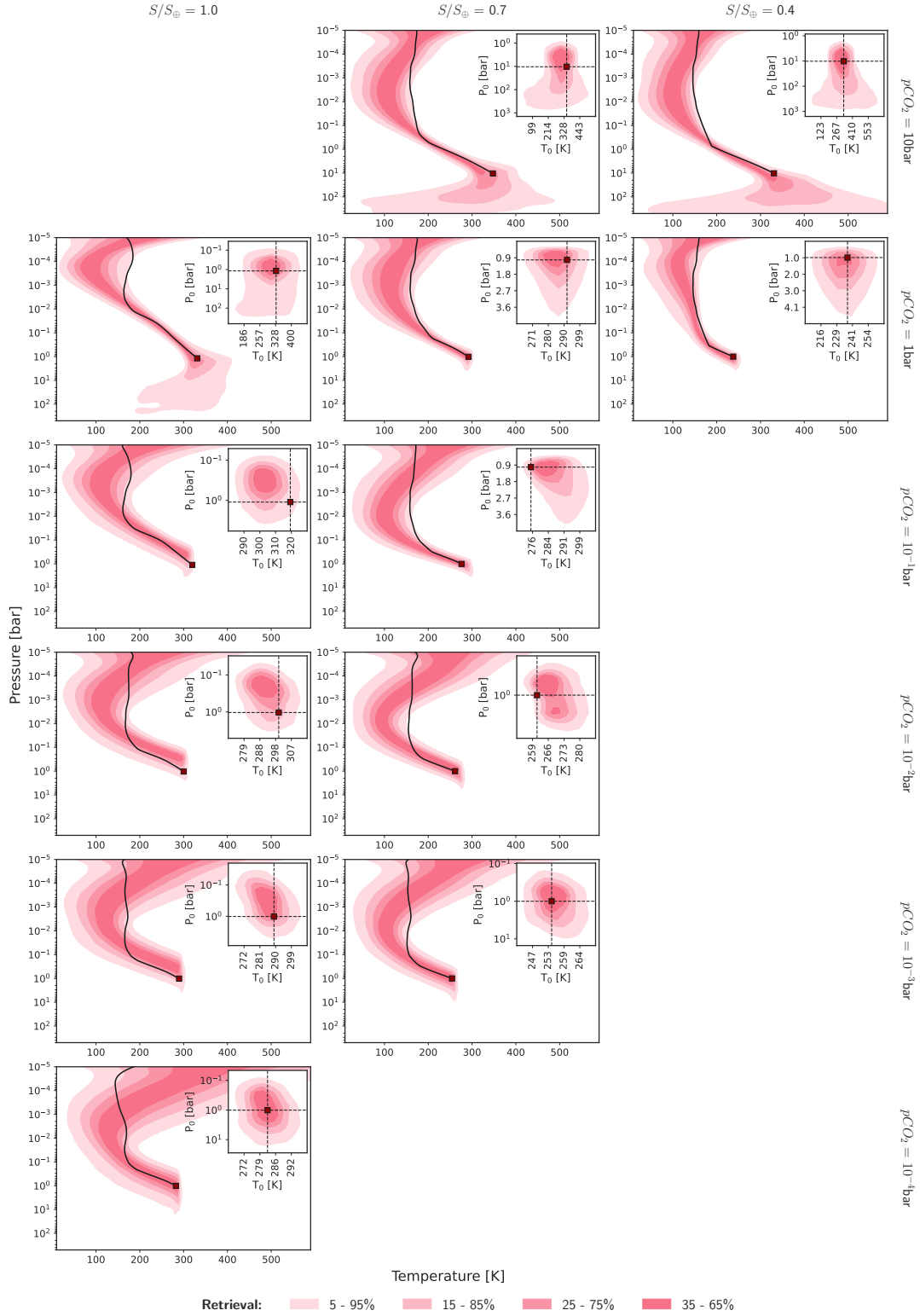


Figure 18. $P - T$ profiles derived from atmospheric spectrum retrievals for $S/N = 10$ and $R = 50$. The panels are arranged to reflect the atmospheric grid within the $p\text{CO}_2$ - S parameter space. Columns represent different stellar insolation values, $S/S_{\oplus} = 1.0, 0.7, 0.4$, while rows correspond to different CO_2 partial pressures, $p\text{CO}_2 = 10\text{ bar}, 1\text{ bar}, 10^{-1}\text{ bar}, 10^{-2}\text{ bar}, 10^{-3}\text{ bar}, 10^{-4}\text{ bar}$. Thick black lines indicate the ground truth $P - T$ profile. The inset shows the retrieved constraints on the surface conditions.

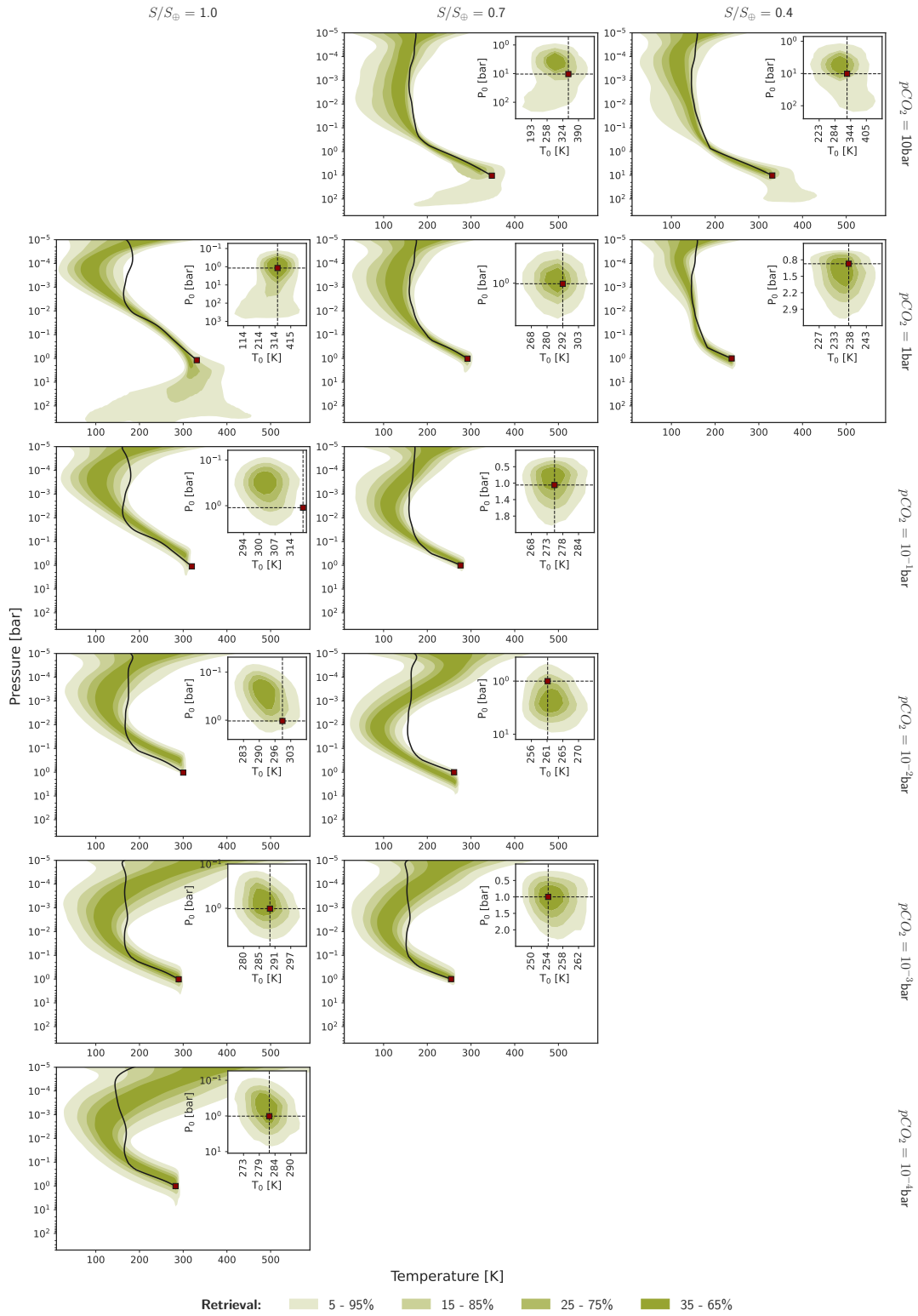


Figure 19. Same as Figure 18 but for $S/N = 10$ and $R = 100$.

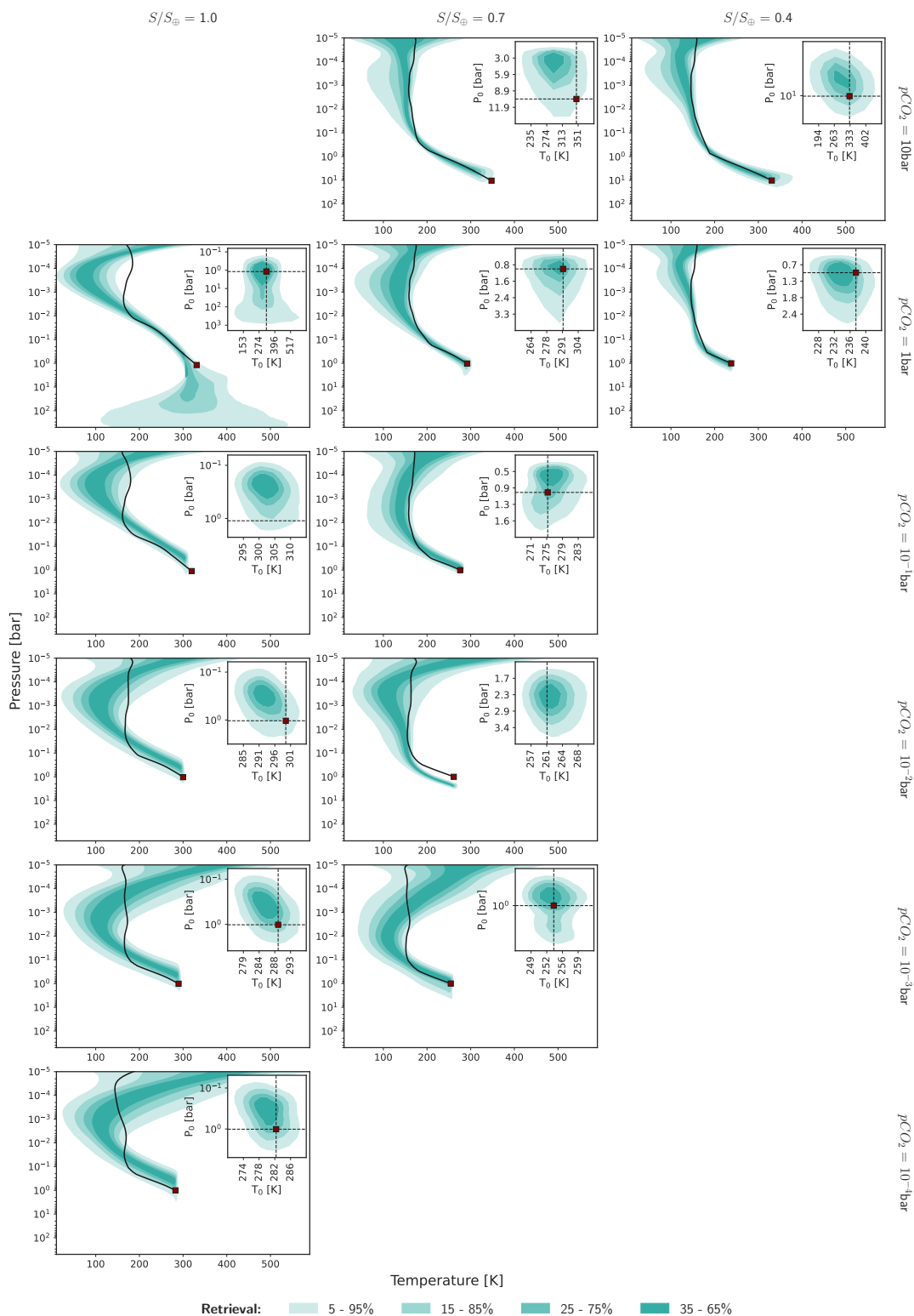


Figure 20. Same as Figure 18 but for $S/N = 20$ and $R = 50$.

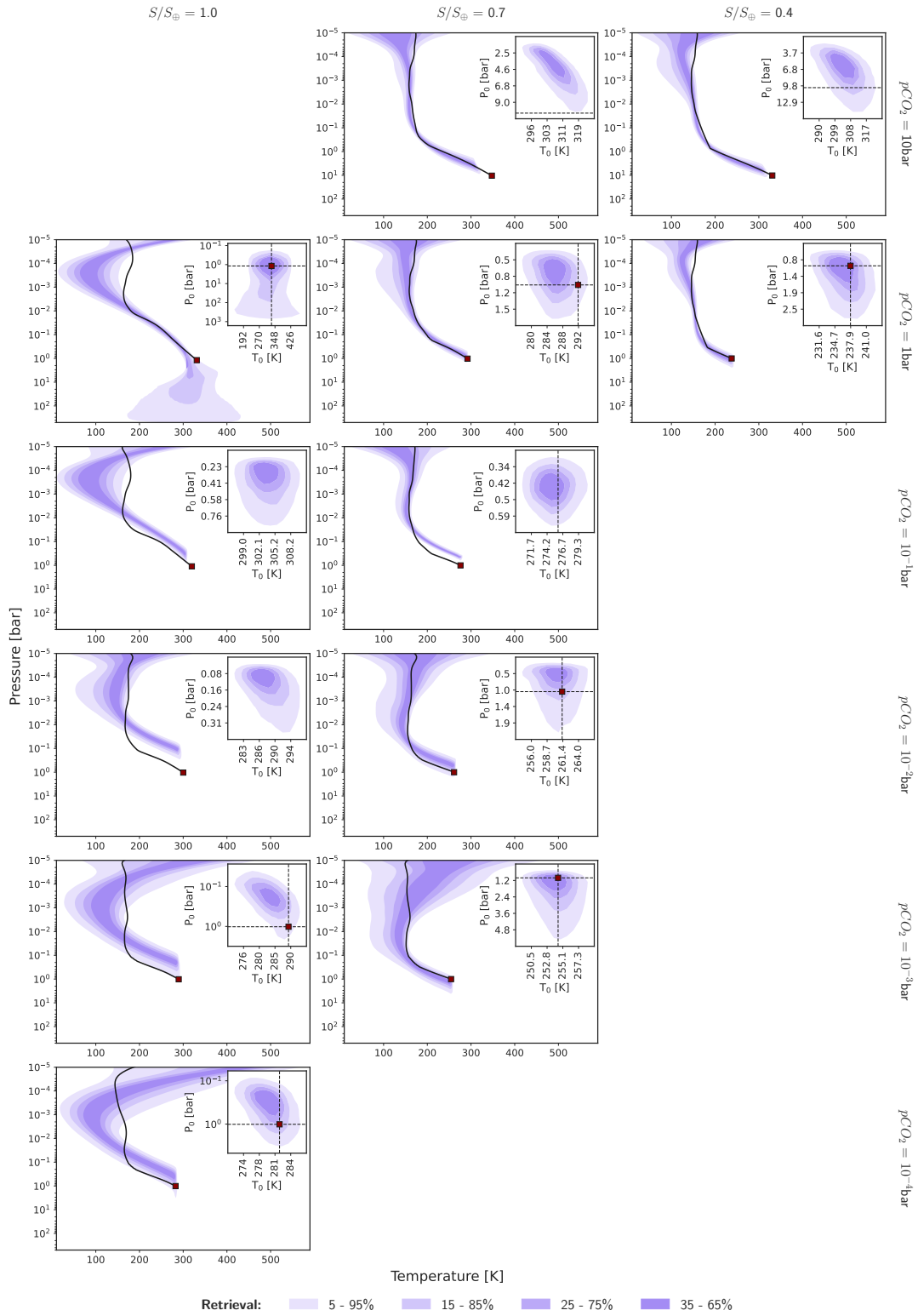


Figure 21. Same as Figure 18 but for $S/N = 20$ and $R = 100$.

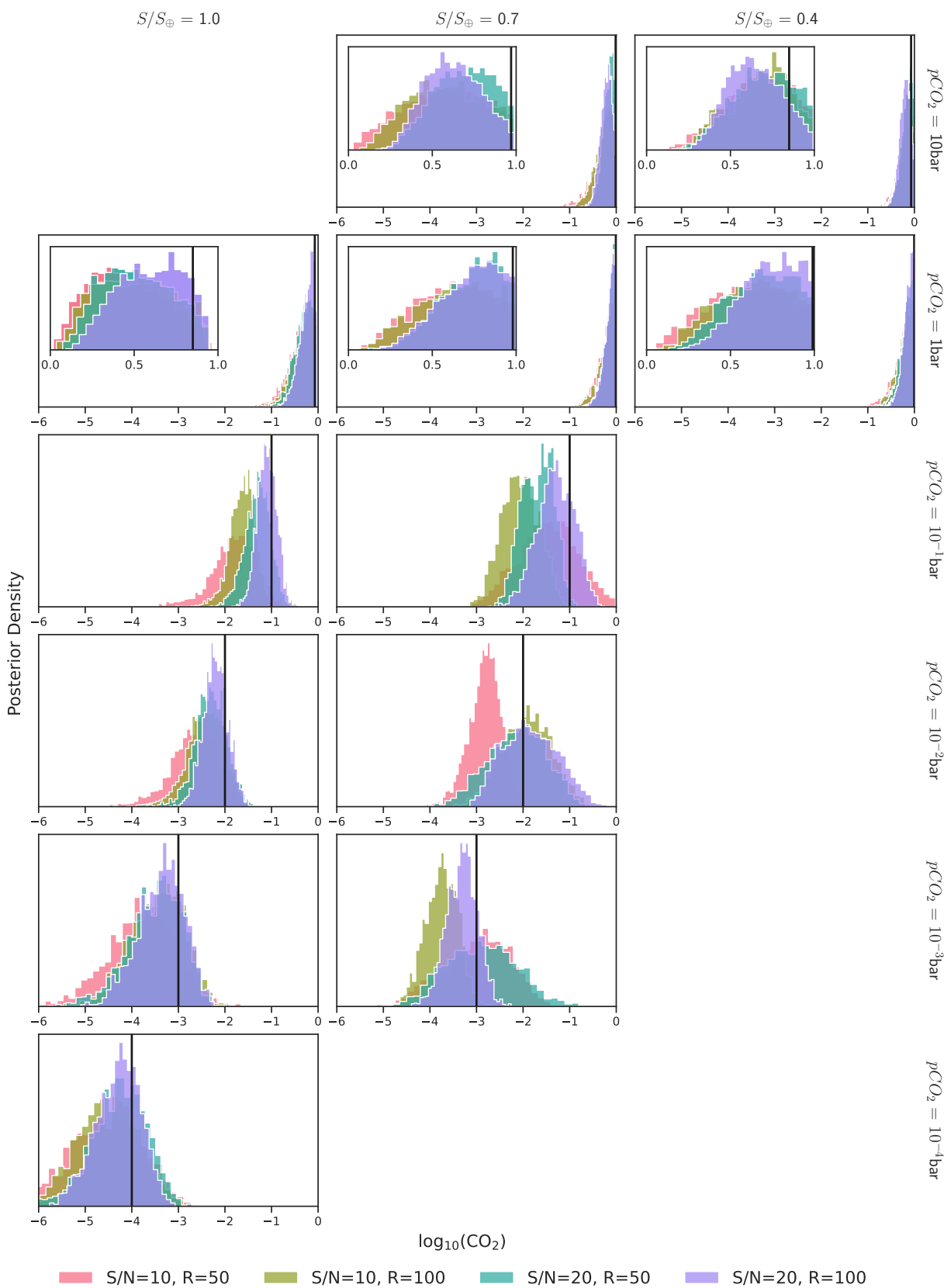


Figure 22. As Figure 5 but for vertically constant H_2O profiles in the input spectra.

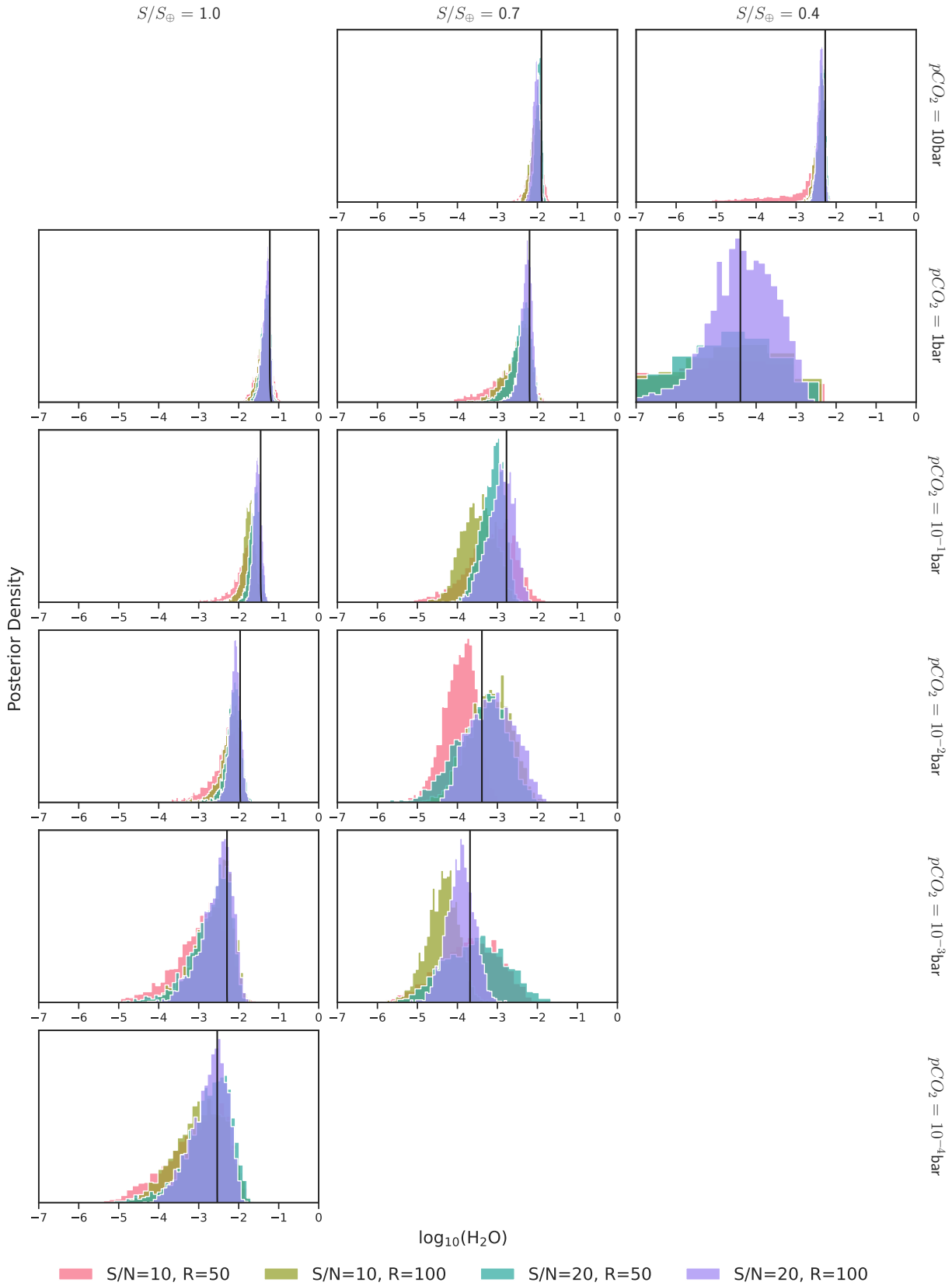


Figure 23. As Figure 17 but for vertically constant H₂O profiles in the input spectra.

C. SUPPLEMENTARY POPULATION TREND RETRIEVAL RESULTS

C.1. Population-Trend Retrieval Results for $S/N = 10$ and $R = 50$

We show retrieved posteriors for trend slope parameter β for the $S/N = 10$ and $R = 50$ case in Figure 24, covering $N_P = [10, 30, 50, 100]$ and both biotic and abiotic scenarios.

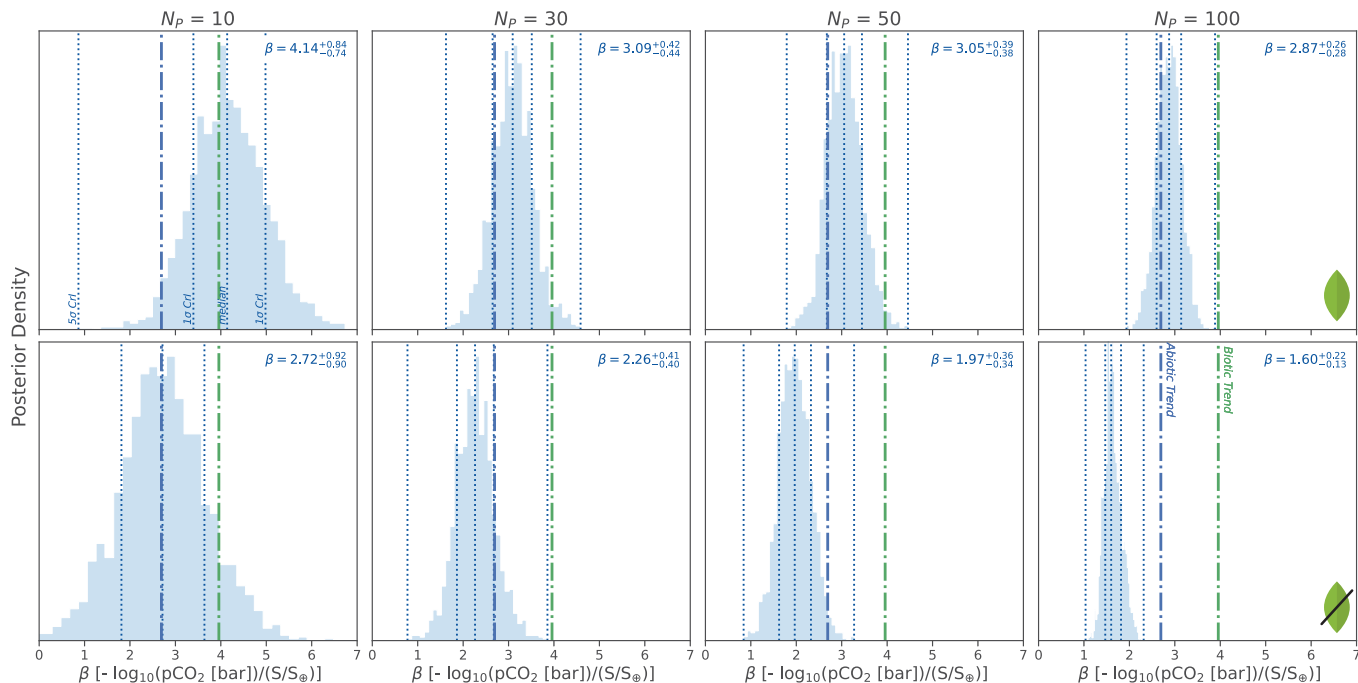


Figure 24. As Figure 8 but for $S/N = 10$ and $R = 50$.

C.2. Jeffreys Scale

We use the Jeffreys scale to quantify model preference and assess the detectability of CO_2 trends by comparing Bayesian evidences, in form of the Bayes' factor K , obtained from our trend inference routine with linear and flat trend models. The Jeffreys scale is presented in Table 3.

Table 3. Jeffreys scale (Jeffreys 1939) for interpretation of the Bayes' factor K .

$\log_{10}(K)$	Probability	Strength of Evidence
< 0	< 0.5	Support for B
0-0.5	0.5-0.75	Weak support for A
0.5-1	0.75-0.91	Substantial support for A
1-2	0.91-0.99	Strong support for A
> 2	> 0.99	Decisive support for A

NOTE—Scale is symmetrical. Hence, negative values of $\log_{10}(K)$ indicate weak, substantial, strong or decisive support for model B.

REFERENCES

- Alei, E., Konrad, B. S., Angerhausen, D., et al. 2022, *A&A*, 665, A106, doi: [10.1051/0004-6361/202243760](https://doi.org/10.1051/0004-6361/202243760)
- Angerhausen, D., Pidhorodetska, D., Leung, M., et al. 2024, *AJ*, 167, 128, doi: [10.3847/1538-3881/ad1f4b](https://doi.org/10.3847/1538-3881/ad1f4b)
- Arney, G., Domagal-Goldman, S. D., Meadows, V. S., et al. 2016, *Astrobiology*, 16, 873, doi: [10.1089/ast.2015.1422](https://doi.org/10.1089/ast.2015.1422)
- Arney, G. N., Meadows, V. S., Domagal-Goldman, S. D., et al. 2017, *ApJ*, 836, 49, doi: [10.3847/1538-4357/836/1/49](https://doi.org/10.3847/1538-4357/836/1/49)
- Arthur, M. A., & Fahey, T. J. 1993, *Soil Science Society of America Journal*, 57, 1122, doi: [10.2136/sssaj1993.03615995005700040040x](https://doi.org/10.2136/sssaj1993.03615995005700040040x)
- Bean, J. L., Abbot, D. S., & Kempton, E. M.-R. 2017, *The Astrophysical Journal Letters*, 841, L24, doi: [10.3847/2041-8213/aa738a](https://doi.org/10.3847/2041-8213/aa738a)
- Bixel, A., & Apai, D. 2021, *AJ*, 161, 228, doi: [10.3847/1538-3881/abe042](https://doi.org/10.3847/1538-3881/abe042)
- Borucki, W. J., Koch, D., Basri, G., et al. 2010, *Science*, 327, 977, doi: [10.1126/science.1185402](https://doi.org/10.1126/science.1185402)
- Bowens, R., Meyer, M. R., Delacroix, C., et al. 2021, *A&A*, 653, A8, doi: [10.1051/0004-6361/202141109](https://doi.org/10.1051/0004-6361/202141109)
- Bryson, S., Kunimoto, M., Kopparapu, R. K., et al. 2021, *The Astronomical Journal*, 161, 36, doi: [10.3847/1538-3881/abc418](https://doi.org/10.3847/1538-3881/abc418)
- Buchner, J. 2016, *PyMultiNest: Python interface for MultiNest*, *Astrophysics Source Code Library*, record ascl:1606.005
- Chapman, S. 1932, *Quarterly Journal of the Royal Meteorological Society*, 58, 11, doi: [10.1002/qj.49705824304](https://doi.org/10.1002/qj.49705824304)
- Charnay, B., Forget, F., Wordsworth, R., et al. 2013, *Journal of Geophysical Research: Atmospheres*, 118, 10,414, doi: <https://doi.org/10.1002/jgrd.50808>
- Checlair, J. 2021, PhD thesis, University of Chicago, Department of Geophysical Sciences
- Chen, J., & Kipping, D. 2016, *The Astrophysical Journal*, 834, 17, doi: [10.3847/1538-4357/834/1/17](https://doi.org/10.3847/1538-4357/834/1/17)
- Dahl, T. W., & Arens, S. K. 2020, *Chemical Geology*, 547, 119665, doi: <https://doi.org/10.1016/j.chemgeo.2020.119665>
- Dannert, F. A., Ottiger, M., Quanz, S. P., et al. 2022, *Astronomy & Astrophysics*, 664, A22, doi: [10.1051/0004-6361/202141958](https://doi.org/10.1051/0004-6361/202141958)
- Ertel, S., Defrère, D., Hinz, P., et al. 2018, *The Astronomical Journal*, 155, 194, doi: [10.3847/1538-3881/aab717](https://doi.org/10.3847/1538-3881/aab717)
- Ertel, S., Defrère, D., Hinz, P., et al. 2020, *The Astronomical Journal*, 159, 177, doi: [10.3847/1538-3881/ab7817](https://doi.org/10.3847/1538-3881/ab7817)
- Faucheux, T. J., Turbet, M., Villanueva, G. L., et al. 2019, *The Astrophysical Journal*, 887, 194, doi: [10.3847/1538-4357/ab5862](https://doi.org/10.3847/1538-4357/ab5862)
- Feroz, F., Hobson, M. P., & Bridges, M. 2009, *Monthly Notices of the Royal Astronomical Society*, 398, 1601, doi: [10.1111/j.1365-2966.2009.14548.x](https://doi.org/10.1111/j.1365-2966.2009.14548.x)
- Forget, F., & Pierrehumbert, R. T. 1997, *Science*, 278, 1273, doi: [10.1126/science.278.5341.1273](https://doi.org/10.1126/science.278.5341.1273)
- Gardner, J. P., Mather, J. C., Abbott, R., et al. 2023, *PASP*, 135, 068001, doi: [10.1088/1538-3873/acd1b5](https://doi.org/10.1088/1538-3873/acd1b5)
- Gaudi, B. S., Seager, S., Mennesson, B., et al. 2020, arXiv e-prints, arXiv:2001.06683, doi: [10.48550/arXiv.2001.06683](https://doi.org/10.48550/arXiv.2001.06683)
- Gebhard, T. D., Angerhausen, D., Konrad, B. S., et al. 2024, *A&A*, 681, A3, doi: [10.1051/0004-6361/202346390](https://doi.org/10.1051/0004-6361/202346390)
- Gordon, I. E., Rothman, L. S., Hargreaves, R. J., et al. 2022, *JQSRT*, 277, 107949, doi: [10.1016/j.jqsrt.2021.107949](https://doi.org/10.1016/j.jqsrt.2021.107949)
- Graham, R. J., & Pierrehumbert, R. 2020, *The Astrophysical Journal*, 896, 115, doi: [10.3847/1538-4357/ab9362](https://doi.org/10.3847/1538-4357/ab9362)
- Grenfell, J. L. 2017, *Physics Reports*, 713, 1, doi: <https://doi.org/10.1016/j.physrep.2017.08.003>
- Hansen, J., Angerhausen, D., Quanz, S. P., et al. 2025, Source Data for Manuscript "Detecting Atmospheric CO₂ Trends as Population-Level Signatures for Long-Term Stable Water Oceans and Biotic Activity on Temperate Terrestrial Exoplanets", Version 1, Zenodo, doi: [10.5281/zenodo.15056424](https://doi.org/10.5281/zenodo.15056424)
- Hao, J., Knoll, A. H., Huang, F., Hazen, R. M., & Daniel, I. 2020, *Geochimica et Cosmochimica Acta*, 273, 70, doi: <https://doi.org/10.1016/j.gca.2020.01.027>
- Harris, C. R., Millman, K. J., van der Walt, S. J., et al. 2020, *Nature*, 585, 357, doi: [10.1038/s41586-020-2649-2](https://doi.org/10.1038/s41586-020-2649-2)
- Harvey, A. H., Gallagher, J. S., & Sengers, J. M. H. L. 1998, *Journal of Physical and Chemical Reference Data*, 27, 761, doi: [10.1063/1.556029](https://doi.org/10.1063/1.556029)
- Hogg, D. W., Myers, A. D., & Bovy, J. 2010, *ApJ*, 725, 2166, doi: [10.1088/0004-637X/725/2/2166](https://doi.org/10.1088/0004-637X/725/2/2166)
- Huber, P. A., Dannert, F. A., Laugier, R., et al. 2024, in *Society of Photo-Optical Instrumentation Engineers (SPIE) Conference Series*, Vol. 13095, *Optical and Infrared Interferometry and Imaging IX*, ed. J. Kammerer, S. Sallum, & J. Sanchez-Bermudez, 130951F, doi: [10.1117/12.3018644](https://doi.org/10.1117/12.3018644)
- Hunter, J. D. 2007, *Computing in Science & Engineering*, 9, 90, doi: [10.1109/MCSE.2007.55](https://doi.org/10.1109/MCSE.2007.55)

- Ibarra, D. E., Rugenstein, J. K. C., Bachan, A., et al. 2019, *American Journal of Science*, 319, 1, doi: [10.2475/01.2019.01](https://doi.org/10.2475/01.2019.01)
- Jeffreys, H. 1939, *Theory of Probability* (Oxford University Press)
- Jones, R. L., Pyle, J. A., Harries, J. E., et al. 1986, *Quarterly Journal of the Royal Meteorological Society*, 112, 1127, doi: [10.1002/qj.49711247412](https://doi.org/10.1002/qj.49711247412)
- Kadoya, S., & Tajika, E. 2014, *The Astrophysical Journal*, 790, 107, doi: [10.1088/0004-637X/790/2/107](https://doi.org/10.1088/0004-637X/790/2/107)
- Kaltenegger, L., Selsis, F., Fridlund, M., et al. 2010, *Astrobiology*, 10, 89, doi: [10.1089/ast.2009.0381](https://doi.org/10.1089/ast.2009.0381)
- Kammerer, J., & Quanz, S. P. 2018, *Astronomy & Astrophysics*, 609, A4, doi: [10.1051/0004-6361/201731254](https://doi.org/10.1051/0004-6361/201731254)
- Kammerer, J., Quanz, S. P., Dannert, F., & LIFE Collaboration. 2022, *Astronomy & Astrophysics*, 668, A52, doi: [10.1051/0004-6361/202243846](https://doi.org/10.1051/0004-6361/202243846)
- Karman, T., Gordon, I. E., van der Avoird, A., et al. 2019, *Icarus*, 328, 160, doi: <https://doi.org/10.1016/j.icarus.2019.02.034>
- Kasper, M., Cerpa Urrea, N., Pathak, P., et al. 2021, *The Messenger*, 182, 38, doi: [10.18727/0722-6691/5221](https://doi.org/10.18727/0722-6691/5221)
- Kasting, J. F., Whitmire, D. P., & Reynolds, R. T. 1993, *Icarus*, 101, 108, doi: [10.1006/icar.1993.1010](https://doi.org/10.1006/icar.1993.1010)
- Kitzmann, D. 2017, *A&A*, 600, A111, doi: [10.1051/0004-6361/201630029](https://doi.org/10.1051/0004-6361/201630029)
- Kitzmann, D., Patzer, A. B. C., von Paris, P., Godolt, M., & Rauer, H. 2011, *A&A*, 534, A63, doi: [10.1051/0004-6361/201117375](https://doi.org/10.1051/0004-6361/201117375)
- Konrad, B. S., Quanz, S. P., Alei, E., & Wordsworth, R. 2024, *ApJ*, 975, 13, doi: [10.3847/1538-4357/ad74f7](https://doi.org/10.3847/1538-4357/ad74f7)
- Konrad, B. S., Alei, E., Quanz, S. P., et al. 2022, *A&A*, 664, A23, doi: [10.1051/0004-6361/202141964](https://doi.org/10.1051/0004-6361/202141964)
- . 2023, *A&A*, 673, A94, doi: [10.1051/0004-6361/202245655](https://doi.org/10.1051/0004-6361/202245655)
- Kopparapu, R. K., Ramirez, R. M., SchottelKotte, J., et al. 2014, *Astrophysical Journal Letters*, 787, L29, doi: [10.1088/2041-8205/787/2/L29](https://doi.org/10.1088/2041-8205/787/2/L29)
- Kopparapu, R. K., Ramirez, R., Kasting, J. F., et al. 2013, *Astrophysical Journal*, 770, 82, doi: [10.1088/0004-637X/770/1/82](https://doi.org/10.1088/0004-637X/770/1/82)
- Krissansen-Totton, J., Arney, G. N., & Catling, D. C. 2018, *Proceedings of the National Academy of Science*, 115, 4105, doi: [10.1073/pnas.1721296115](https://doi.org/10.1073/pnas.1721296115)
- Krissansen-Totton, J., & Catling, D. C. 2017, *Nature Communications*, 8, 15423, doi: [10.1038/ncomms15423](https://doi.org/10.1038/ncomms15423)
- Krissansen-Totton, J., Garland, R., Irwin, P., & Catling, D. C. 2018, *The Astronomical Journal*, 156, 114, doi: [10.3847/1538-3881/aad564](https://doi.org/10.3847/1538-3881/aad564)
- Lehmer, O. R., Catling, D. C., & Krissansen-Totton, J. 2020, *Nature Communications*, 11, 6153, doi: [10.1038/s41467-020-19896-2](https://doi.org/10.1038/s41467-020-19896-2)
- Lehmer, O. R., Catling, D. C., & Krissansen-Totton, J. 2020, *Supplementary Software for Carbonate-silicate cycle predictions of Earth-like planetary climates and testing the habitable zone concept*. <https://www.nature.com/articles/s41467-020-19896-2>
- Lustig-Yaeger, J., Sotzen, K. S., Stevenson, K. B., et al. 2022, *The Astronomical Journal*, 163, 140, doi: [10.3847/1538-3881/ac5034](https://doi.org/10.3847/1538-3881/ac5034)
- Madhusudhan, N. 2018, *Atmospheric Retrieval of Exoplanets* (Cham: Springer International Publishing), 2153–2182, doi: [10.1007/978-3-319-55333-7_104](https://doi.org/10.1007/978-3-319-55333-7_104)
- Manabe, S., & Wetherald, R. T. 1967, *Journal of the Atmospheric Sciences*, 24, 241, doi: [10.1175/1520-0469\(1967\)024<0241:TEOTAW>2.0.CO;2](https://doi.org/10.1175/1520-0469(1967)024<0241:TEOTAW>2.0.CO;2)
- Marley, M. S., Ackerman, A. S., Cuzzi, J. N., & Kitzmann, D. 2013, *Clouds and hazes in exoplanet atmospheres*, *Space Science Series* (Phoenix: University of Arizona Press), 367–391, doi: [10.2458/azu_uapress_9780816530595-ch015](https://doi.org/10.2458/azu_uapress_9780816530595-ch015)
- Meadows, V. S. 2008, in *Exoplanets*, ed. J. W. Mason (Springer), 259, doi: [10.1007/978-3-540-74008-7_10](https://doi.org/10.1007/978-3-540-74008-7_10)
- Menti, F., Caballero, J. A., Wyatt, M. C., et al. 2024, *Research Notes of the American Astronomical Society*, 8, 267, doi: [10.3847/2515-5172/ad887e](https://doi.org/10.3847/2515-5172/ad887e)
- Mettler, J.-N., Konrad, B. S., Quanz, S. P., & Helled, R. 2024, *ApJ*, 963, 24, doi: [10.3847/1538-4357/ad198b](https://doi.org/10.3847/1538-4357/ad198b)
- Miller, D. W., Morgan, R. M., & de Weck, O. L. 2024, in *Society of Photo-Optical Instrumentation Engineers (SPIE) Conference Series*, Vol. 13099, *Modeling, Systems Engineering, and Project Management for Astronomy XI*, ed. S. E. Egner & S. Roberts, 1309919, doi: [10.1117/12.3018535](https://doi.org/10.1117/12.3018535)
- Misra, A., Meadows, V., Claire, M., & Crisp, D. 2014, *Astrobiology*, 14, 67, doi: [10.1089/ast.2013.0990](https://doi.org/10.1089/ast.2013.0990)
- Mollière, P., Wardenier, J. P., van Boekel, R., et al. 2019, *A&A*, 627, A67, doi: [10.1051/0004-6361/201935470](https://doi.org/10.1051/0004-6361/201935470)
- Mollière, P., Stölker, T., Lacour, S., et al. 2020, *A&A*, 640, A131, doi: [10.1051/0004-6361/202038325](https://doi.org/10.1051/0004-6361/202038325)
- Morley, C. V., Kreidberg, L., Rustamkulov, Z., Robinson, T., & Fortney, J. J. 2017, *The Astrophysical Journal*, 850, 121, doi: [10.3847/1538-4357/aa927b](https://doi.org/10.3847/1538-4357/aa927b)
- Moulton, K. L. 2000, *American Journal of Science*, 300, 539, doi: [10.2475/ajs.300.7.539](https://doi.org/10.2475/ajs.300.7.539)

- National Academies of Sciences, and Medicine, Engineering. 2021, *Pathways to Discovery in Astronomy and Astrophysics for the 2020s* (The National Academies Press), doi: [10.17226/26141](https://doi.org/10.17226/26141)
- Peterson, B. M., Fischer, D., & LUVOIR Science and Technology Definition Team. 2017, in *American Astronomical Society Meeting Abstracts*, Vol. 229, *American Astronomical Society Meeting Abstracts #229*, 405.04
- Porder, S. 2019, *Elements*, 15, 241, doi: [10.2138/gselements.15.4.241](https://doi.org/10.2138/gselements.15.4.241)
- Quanz, S. P., Crossfield, I., Meyer, M. R., Schmalzl, E., & Held, J. 2015, *International Journal of Astrobiology*, 14, 279, doi: [10.1017/S1473550414000135](https://doi.org/10.1017/S1473550414000135)
- Quanz, S. P., Absil, O., Benz, W., et al. 2022a, *Experimental Astronomy*, 54, 1197, doi: [10.1007/s10686-021-09791-z](https://doi.org/10.1007/s10686-021-09791-z)
- Quanz, S. P., Ottiger, M., Fontanet, E., et al. 2022b, *A&A*, 664, A21, doi: [10.1051/0004-6361/202140366](https://doi.org/10.1051/0004-6361/202140366)
- Ricker, G. R., Winn, J. N., Vanderspek, R., et al. 2015, *Journal of Astronomical Telescopes, Instruments, and Systems*, 1, 014003, doi: [10.1117/1.JATIS.1.1.014003](https://doi.org/10.1117/1.JATIS.1.1.014003)
- Rugheimer, S., & Kaltenegger, L. 2018, *ApJ*, 854, 19, doi: [10.3847/1538-4357/aaa47a](https://doi.org/10.3847/1538-4357/aaa47a)
- Sagan, C., & Mullen, G. 1972, *Science*, 177, 52, doi: [10.1126/science.177.4043.52](https://doi.org/10.1126/science.177.4043.52)
- Schlecker, M., Apai, D., Lichtenberg, T., et al. 2024, *The Planetary Science Journal*, 5, 3, doi: [10.3847/PSJ/acf57f](https://doi.org/10.3847/PSJ/acf57f)
- Schwieterman, E. W., & Leung, M. 2024, *Reviews in Mineralogy and Geochemistry*, 90, 465, doi: [10.2138/rmg.2024.90.13](https://doi.org/10.2138/rmg.2024.90.13)
- Schwieterman, E. W., Robinson, T. D., Meadows, V. S., Misra, A., & Domagal-Goldman, S. 2015, *ApJ*, 810, 57, doi: [10.1088/0004-637X/810/1/57](https://doi.org/10.1088/0004-637X/810/1/57)
- Schwieterman, E. W., Kiang, N. Y., Parenteau, M. N., et al. 2018, *Astrobiology*, 18, 663, doi: [10.1089/ast.2017.1729](https://doi.org/10.1089/ast.2017.1729)
- Sneep, M., & Ubachs, W. 2005, *Journal of Quantitative Spectroscopy and Radiative Transfer*, 92, 293, doi: <https://doi.org/10.1016/j.jqsrt.2004.07.025>
- Stark, C. C., Belikov, R., Bolcar, M. R., et al. 2019, *Journal of Astronomical Telescopes, Instruments, and Systems*, 5, 024009, doi: [10.1117/1.JATIS.5.2.024009](https://doi.org/10.1117/1.JATIS.5.2.024009)
- Tajika, E., & Matsui, T. 1992, *Earth and Planetary Science Letters*, 113, 251, doi: [https://doi.org/10.1016/0012-821X\(92\)90223-I](https://doi.org/10.1016/0012-821X(92)90223-I)
- Tajika, E., & Matsui, T. 1993, *Lithos*, 30, 267, doi: [10.1016/0024-4937\(93\)90040-J](https://doi.org/10.1016/0024-4937(93)90040-J)
- Thalman, R., Zarzana, K. J., Tolbert, M. A., & Volkamer, R. 2014, *JQSRT*, 147, 171, doi: [10.1016/j.jqsrt.2014.05.030](https://doi.org/10.1016/j.jqsrt.2014.05.030)
- . 2017, *JQSRT*, 189, 281, doi: [10.1016/j.jqsrt.2016.12.014](https://doi.org/10.1016/j.jqsrt.2016.12.014)
- The LUVOIR Team. 2019, arXiv e-prints, arXiv:1912.06219, doi: [10.48550/arXiv.1912.06219](https://doi.org/10.48550/arXiv.1912.06219)
- TRAPPIST-1 JWST Community Initiative, de Wit, J., Doyon, R., et al. 2024, *Nature Astronomy*, 8, 810, doi: [10.1038/s41550-024-02298-5](https://doi.org/10.1038/s41550-024-02298-5)
- Virtanen, P., Gommers, R., Oliphant, T. E., et al. 2020, *Nature Methods*, 17, 261, doi: [10.1038/s41592-019-0686-2](https://doi.org/10.1038/s41592-019-0686-2)
- Walker, J. C. G., Hays, P. B., & Kasting, J. F. 1981, *Journal of Geophysical Research: Oceans*, 86, 9776, doi: <https://doi.org/10.1029/JC086iC10p09776>
- Wes McKinney. 2010, in *Proceedings of the 9th Python in Science Conference*, ed. Stéfan van der Walt & Jarrod Millman, 56 – 61, doi: [10.25080/Majora-92bf1922-00a](https://doi.org/10.25080/Majora-92bf1922-00a)
- Wolf, E. T., Shields, A. L., Kopparapu, R. K., Haqq-Misra, J., & Toon, O. B. 2017, *The Astrophysical Journal*, 837, 107, doi: [10.3847/1538-4357/aa5ffc](https://doi.org/10.3847/1538-4357/aa5ffc)
- Wordsworth, R., & Kreidberg, L. 2022, *Annual Review of Astronomy and Astrophysics*, 60, 159, doi: <https://doi.org/10.1146/annurev-astro-052920-125632>